

Observational signatures of the dust size evolution in isolated galaxy simulations

Kosei Matsumoto^{1,2,3,*}, Hiroyuki Hirashita^{4,5}, Kentaro Nagamine^{5,6,7}, Stefan van der Giessen^{1,8}, Leonard E. C. Romano^{9,10,11}, Monica Relaño^{8,12}, Ilse De Looze¹, Maarten Baes¹, Angelos Nersesian^{1,13}, Peter Camps¹, Kuan-chou Hou¹⁴, and Yuri Oku⁵

¹ Sterrenkundig Observatorium Department of Physics and Astronomy Universiteit Gent, Krijgslaan 281 S9, B-9000 Gent, Belgium

² Department of Physics, Graduate School of Science, The University of Tokyo, 7-3-1 Hongo, Bunkyo-ku, Tokyo 113-0033, Japan

³ Institute of Space and Astronautical Science, Japan Aerospace Exploration Agency, 3-1-1 Yoshinodai, Chuo-ku, Sagami-hara, Kanagawa 252-5210, Japan

⁴ Institute of Astronomy and Astrophysics, Academia Sinica, Astronomy-Mathematics Building, No. 1, Section 4, Roosevelt Road, Taipei 10617, Taiwan

⁵ Theoretical Astrophysics, Department of Earth and Space Science, Osaka University, 1-1 Machikaneyama, Toyonaka, Osaka 560-0043, Japan

⁶ Kavli IPMU (WPI), The University of Tokyo, 5-1-5 Kashiwanoha, Kashiwa, Chiba 277-8583, Japan

⁷ Department of Physics and Astronomy, University of Nevada, Las Vegas, 4505 S. Maryland Pkwy, Las Vegas, NV 89154-4002, USA

⁸ Dept. Física Teórica y del Cosmos, Universidad de Granada, Spain

⁹ Universitäts-Sternwarte, Fakultät für Physik, Ludwig-Maximilians-Universität München, Scheinerstr. 1, D-81679 München, Germany

¹⁰ Max-Planck-Institut für extraterrestrische Physik, Giessenbachstr. 1, D-85741 Garching, Germany

¹¹ Excellence Cluster ORIGINS, Boltzmannstr. 2, D-85748 Garching, Germany

¹² Instituto Universitario Carlos I de Física Teórica y Computacional, Universidad de Granada, 18071, Granada, Spain

¹³ STAR Institute, Université de Liège, Quartier Agora, Allée du six Aout 19c, B-4000 Liege, Belgium

¹⁴ Physics Department, Ben-Gurion University of the Negev, Be'er-Sheva 84105, Israel

Received February 6, 2024

ABSTRACT

Aims. We aim at providing observational signatures of the dust size evolution in the ISM, in particular exploring indicators of polycyclic aromatic hydrocarbon (PAH) mass fraction (q_{PAH}) defined as the mass fraction of PAHs relative to total dust grains. Additionally, we validate our dust evolution model by comparing the observational signatures from our simulations to those from observations.

Methods. We model dust properties of Milky Way-like and NGC 628-like galaxies representing star-forming galaxies with a hydrodynamic simulation code, GADGET4-OSAKA, which incorporates the evolution of grain size distribution driven by dust production and interstellar processing. Furthermore, we perform post-processing dust radiative transfer calculations with SKIRT based on the hydrodynamic simulations to predict the observational properties of the simulations.

Results. We find that the intensity ratio between $8\ \mu\text{m}$ and $24\ \mu\text{m}$ ($I_{\nu}(8\ \mu\text{m})/I_{\nu}(24\ \mu\text{m})$) correlates with q_{PAH} and can be used as an indicator of PAH mass fraction. However, this ratio is influenced by the local radiation field. As another indicator of PAH mass fraction, we suggest the $8\ \mu\text{m}$ -to-total infrared intensity ratio ($\nu I_{\nu}(8\ \mu\text{m})/I_{\text{TIR}}$), which tightly correlates with the PAH mass fraction. Furthermore, we explore the spatial evolution of the PAH mass fraction in the simulated Milky Way-like galaxy using $\nu I_{\nu}(8\ \mu\text{m})/I_{\text{TIR}}$. We find that the spatially resolved PAH mass fraction increases with metallicity in a lower metallicity regime ($Z \lesssim 0.2 Z_{\odot}$) due to the interplay between accretion and shattering while it decreases with metallicity in a high metallicity regime ($Z \gtrsim 0.2 Z_{\odot}$) due to coagulation process. Also, the coagulation decreases the PAH mass fraction in regions with a high hydrogen surface density. Finally, we compare the above indicators in the NGC 628-like simulation with those observed in NGC 628 by *Herschel*, *Spitzer*, and *JWST*. Consequently, we find that our simulation underestimates the PAH mass fraction throughout the entire galaxy. This is probably because PAH is too efficiently lost by coagulation in the interstellar medium in our model, which suggests that the inhibition of coagulation of the PAHs in the ISM is a key to enhancing PAH formation in our model.

Key words. Radiative transfer – ISM: molecules – Dust extinction – Methods: numerical

1. Introduction

Dust in the interstellar medium (ISM) plays a key role in shaping the observed properties of galaxies as well as indirectly affecting galaxy evolution. Dust governs various radiative processes

in galaxies: dust absorbs and scatters ultraviolet (UV) and optical light from young stars, and reemits that light as infrared (IR) radiation. These processes are reflected in the spectral energy distributions (SEDs) of galaxies; thus, analysis of the UV-to-IR SEDs of galaxies provides various clues to their physical properties such as star formation rate (SFR) and dust mass (e.g., [Conroy](#)

* e-mail: kosei.matsumoto@ugent.be

2013). In addition, dust grains provide favorable conditions for the formation of hydrogen molecules through the grain-surface reaction, and shielding of UV radiation from stars by dust grains suppresses the dissociation of molecular hydrogen (Hollenbach & Salpeter 1971; Hollenbach & McKee 1979; Cazaux & Tielens 2004; Grieco et al. 2023). Such a molecular-rich environment is favorable for star formation, with dust acting as a cooling channel in molecular clouds (Ostriker & Silk 1973; Vogelsberger et al. 2019). On the contrary, the photoelectric heating by dust grains is the main heating source of the photodissociation and X-ray dissociation regions in the ISM, changing the ISM conditions and causing chemical reactions (Tielens & Hollenbach 1985; Maloney et al. 1996; Wolfire et al. 2022). Therefore, dust is a crucial component of galaxy formation and evolution.

To derive dust properties in the nearby universe, many observational studies have been performed by analyzing SEDs with IR photometric data after the appearance of *Herschel* and *Spitzer* telescopes, which cover wavelengths of 3–670 μm (e.g., da Cunha et al. 2008; Leja et al. 2017; Nersesian et al. 2019; Burgarella et al. 2020). Observed galaxy IR SEDs reflect the grain temperatures dependent on the grain size (including the stochastic heating; Draine & Anderson 1985) and the material-dependent emission features at certain wavelengths. In particular, the most prominent features seen at $\sim 3\text{--}20 \mu\text{m}$ are considered to originate from PAH bands (Li & Draine 2001; Draine & Li 2007; Li 2020). Thus, the SED fitting analysis is capable of extracting the grain size distribution and the PAH abundance (Galliano et al. 2008b, 2021; Relaño et al. 2020, 2022). Rémy-Ruyer et al. (2015) reveal an increasing trend of PAH mass fraction, which is defined as the mass fraction of PAHs relative to total dust grains, with respect to metallicity (see also Draine et al. 2007; Aniano et al. 2020; Shim et al. 2023). Seok et al. (2014) suggest that PAHs are produced by the shattering of carbonaceous grains, which form more efficiently by the accretion of metals on dust grains in regions with higher metallicity, naturally explaining the increasing trend of PAH mass fraction against metallicity. Chastenot et al. (2019) investigate the PAH mass fraction with spatially resolved data of the Small and Large Magellanic Clouds (SMC and LMC, respectively) and find a higher PAH mass fraction in the diffuse medium in the LMC compared to that in the SMC. To explain this result, they suggest shattering large grains to PAHs is preferable to other PAH formation scenarios (e.g., PAH formation in the envelope of asymptotic giant branch (AGB) stars; Cherchneff et al. 1992; Sloan et al. 2008, 2014; Matsuura et al. 2014) and that the shattering works more efficiently in the LMC with higher metallicity. Therefore, these observations using PAH features provide us clues to understanding dust processes in various ISM.

In the SED fitting methods, however, the spatial resolutions of the photometric data are always reduced to the worst one, compromising the spatial dust characteristics obtained. Photometric and spectroscopic observations with only a few prominent PAH emission features are useful to derive more detailed spatial PAH properties (mass, size, and ionization), offering a more comprehensive understanding of dust processes in the ISM (Li 2020). Today, the James Webb Space Telescope (*JWST*) starts to investigate spatially resolved PAH features of several nearby galaxies. Egorov et al. (2023) suggest the intensity ratio of the emission at 7.7 and 11.3 μm to the 21 μm emission (R_{PAH}) for an indicator of the PAH mass fraction given by

$$R_{\text{PAH}} = \frac{I_{\nu}(7.7 \mu\text{m}) + I_{\nu}(11.3 \mu\text{m})}{I_{\nu}(21 \mu\text{m})}. \quad (1)$$

They find that R_{PAH} decreases with the ionization fraction and implies that PAH destruction by UV radiation works in the star-forming regions. Chastenot et al. (2023b) exhibit a decreasing trend of the 3.35 to 11.3 μm intensity ratio against molecular gas fraction, implying that larger grains are more abundant in denser regions. Although those observations imply the spatially resolved dust processes in the ISM, it is difficult to quantitatively infer the actual dust properties such as mass and grain sizes. Therefore, to interpret those observations and discuss the dust processes in ISM, it is essential to theoretically model dust evolution and compare observational signatures of the dust evolution of the model to those of observations.

In the past decades, many studies have been conducted on dust evolution using physically motivated one-zone models (e.g., Lisenfeld & Ferrara 1998; Dwek 1998; Hirashita 1999). Essentially, it calculates grain size distributions for predictions of dust signatures in extinction curves and dust emission in SEDs. Some models describe the evolution of grain size distribution (e.g., O’Donnell & Mathis 1997; Asano et al. 2013; Hirashita & Aoyama 2019), which have indeed been used to predict extinction curves. Hirashita et al. (2020); Nishida et al. (2022) investigate the evolution of the dust emission SED based on the model of grain size distribution.

Today, these evolution models of grain size distributions, including a simplified two-size approximation (Hirashita 2015), have been applied to hydrodynamical simulations (McKinnon et al. 2018; Aoyama et al. 2017, 2020; Hou et al. 2019; Graziani et al. 2020; Granato et al. 2021; Romano et al. 2022a; Narayanan et al. 2023) to calculate the evolution of dust content in galaxies in a manner consistent with the hydrodynamic evolution of the ISM. Among them, Aoyama et al. (2020) solve the evolution of grain size distribution represented by 32-grain radius bins in an isolated galaxy simulation with a hydrodynamic simulation code, GADGET3-OSAKA, and find that the grain size distribution depends on the physical condition (especially density and metallicity) of ambient ISM. This result underlines the importance of solving the grain size distribution in a manner consistent with the hydrodynamical and chemical evolution of the ISM. Romano et al. (2022a) extend their models with more sophisticated sub-grid models, in which the fraction on a sub-grid scale is varied according to the ambient density, and dust diffusion between SPH gas particles (hereafter, gas particles) is taken into account. In particular, they show that the inhomogeneity in the grain size distribution in the ISM is strongly affected by the treatment of diffusion. These simulations broadly succeed in reproducing the Milky Way extinction curve and predicting the evolution of grain size distribution, but they have not studied the influences of the radiative processes on the observational properties based on the stellar and dust distribution of the hydrodynamic simulations.

Narayanan et al. (2023) employ hydrodynamical simulations and post-processing radiative transfer calculations, which handle the grain size distributions and dust composition including PAHs, and investigate characteristics of dust emission in different types of galaxies. They find a significant influence of the radiation field on the ratio between global PAH luminosity and mass, inferring the importance of the radiative processes to derive actual dust properties in observations. However, it is still uncertain how the effect of radiative processes can be canceled out in observations, and observational signatures for deriving dust processes, which are not affected by the radiation field, are unknown. Therefore, it is crucial to investigate how grain size distributions are reflected on IR spectral features in simulations and infer observational signatures, which can be directly compared with those in observations.

In this paper, we model the evolution of grain size distribution in isolated galaxies with hydrodynamic simulations (Romano et al. 2022a) and perform radiative transfer calculations by taking into account the grain size distributions and different grain species such as silicate, carbonaceous dust grains, and PAHs in post-processing. Here, we assume that the main driver of PAH formation is the shattering of large carbonaceous grains, which is implied by both observational and theoretical studies (Chasnet et al. 2019; Seok et al. 2014; Rau et al. 2019; Hirashita & Murga 2020; Narayanan et al. 2023). We focus on two isolated galaxy simulations representing star-forming galaxies similar to the Milky Way and NGC 628. The Milky Way-like galaxy is well-studied in different types of simulations as a typical star-forming galaxy in explaining the impact of their subgrid models on the galaxy evolution (Kim et al. 2016; Shimizu et al. 2019; Romano et al. 2022a,b). The Milky Way-like galaxy encapsulates a broad range of gas densities and metallicities, rendering it an apt experimental setup to probe the long-term dust evolution and the impact of the evolution on observable properties. On the other hand, NGC 628 is among the most extensively studied galaxies in observations of the nearby universe, offering high spatial resolutions in the PHANGS surveys (Kennicutt et al. 2011; Leroy et al. 2021; Lee et al. 2023). NGC 628 is one of the most nearby galaxies and a nearly face-on galaxy, allowing us to separately study dust processes in diffuse and dense ISM with minimal interference from dust extinction. Furthermore, NGC 628 is a moderately star-forming galaxy without the signature of the active galactic nucleus observed in the *JWST* program 2107 (PI: J. Lee; Lee et al. 2023). Therefore, comparing the observable properties of NGC 628 between the simulation and observations serves as a robust test to validate the dust evolution model, particularly within the context of star-forming galaxies. More comprehensive comparisons including other nearby galaxies will be presented in our future work (van der Giessen et al. in preparation).

The main goals of this paper are the following: (i) We explore what drives the variations of grain size distributions and PAH abundances in different galaxy environments. (ii) We spatially investigate how dust evolution is reflected in SEDs and dust emission at various stages of galaxy evolution. (iii) We infer and validate various indicators of PAH mass fractions in ISM by making spatial comparisons with the actual PAH mass fraction in hydrodynamic simulations. (iv) We validate our dust evolution model by spatially comparing the indicators of the PAH mass fraction between the NGC 628-like galaxy simulation and actual observations.

This paper is organized as follows. Section 2 describes the models in our hydrodynamic simulations of GADGET4-OSAKA, post-processing radiative transfer calculations by SKIRT, and the observational analysis. In Section 3, we explore the differences of the dust evolution and PAH abundance between the Milky Way- and NGC 628-like galaxies. In Section 4, we investigate the evolution of the spectral features in SEDs of the Milky Way-like galaxy and indicators of the PAH mass fraction using intensity ratios at various wavelengths. In Section 5, we perform spatially resolved comparisons for the indicators of the PAH mass fraction between observations and simulations, and discuss additional physical processes required for our dust model. In Section 6, we give our conclusions.

2. Methods

2.1. Isolated galaxy simulations

To perform isolated galaxy simulations, we use a smooth particle hydrodynamic (SPH) simulation code, GADGET4-OSAKA (Romano et al. 2022a,b), which is a modified version of GADGET4 (Springel et al. 2021). GADGET4-OSAKA incorporates the OSAKA feedback model along with a dust evolution model (Aoyama et al. 2020; Romano et al. 2022a,b). The integrated feedback and dust models allow us to approach a self-consistent treatment of star formation, feedback processes, and metal/dust formation within the context of hydrodynamic evolution in galaxies. Here, we briefly summarize those models and refer the reader to the references for more details.

The star formation and feedback processes are incorporated into our code as subgrid prescriptions. Star formation occurs stochastically, guided by a star formation efficiency of $\epsilon_s = 0.05$ that follows the Kennicutt-Schmidt law (Kennicutt 1998). This process is initiated when gas particles satisfy certain conditions, specifically when $n_H > 20 \text{ cm}^{-3}$ and $T_{\text{gas}} < 10^4 \text{ K}$ (n_H is the hydrogen number density and T_{gas} is the gas temperature) are satisfied. The Osaka feedback model distinctly addresses the feedback processes of Type Ia supernovae (SNe), Type II SNe, asymptotic giant branch (AGB) stars, and young stars. The model manages energy ejections from both thermal and kinetic feedback modes (Shimizu et al. 2019). Additionally, SNe and AGB stars eject various metal elements and the ejected metal mass is calculated using the CELib library (Saitoh 2017). Moreover, we utilize the GRACKLE-3 radiative cooling library (Smith et al. 2017)¹, which solves the non-equilibrium primordial chemical network (H, He, and D), taking into account metal cooling as well as photo-heating and photo-ionization due to the UV background (Haardt & Madau 2012).

The dust evolution model adopted by Romano et al. (2022a) is an enhanced version of those used by Hirashita & Aoyama (2019) and Aoyama et al. (2020). We calculate the grain size distribution in each gas particle. This implicitly assumes a perfect dynamic coupling between dust and gas within each gas particle. The grains are assumed to be compact spheres with material density s , such that the grain mass m and radius a are related as $m = \frac{4}{3}\pi a^3 s$. The grain size distribution, denoted as $n(a)$, is defined so that $n(a) da$ is the number density of grains whose radii are between a and $a + da$. We consider the grain radii ranging from 3.0×10^{-4} to $10 \mu\text{m}$ with 30 logarithmically spaced discrete bins. In our simulations, AGB stars and SNe produce large dust grains. Here, 10% of the ejected metals from AGB stars and SNe are assumed to condense into dust grains with a log-normal grain size distribution characterized by the mean grain radius of $0.1 \mu\text{m}$ and variance of 0.47 (Asano et al. 2013). Our model also takes into account a variety of interstellar dust processes including shattering and thermal sputtering in the diffuse ISM and dust size growth through accretion and coagulation in the dense ISM (Aoyama et al. 2020). Dust destruction in SN shocks and metal/dust diffusion between the diffuse and dense ISM are also considered.

Furthermore, We note that our simulations do not have sufficient spatial resolutions for cold and dense gas ($T_{\text{gas}} < 50 \text{ K}$ and $n_H > 10^3 \text{ cm}^{-3}$), which could cause inefficient coagulation and accretion processes. Thus, Romano et al. (2022a) employ a two-phase ISM subgrid model for gas particles, where it is assumed that dense and diffuse gas media co-exist in each gas particle.

¹ <https://grackle.readthedocs.org/>

Table 1: Properties of each component laid in the initial conditions of the Milky Way-like and NGC 628-like galaxy simulations

Components	Milky Way-like		NGC 628-like	
	Mass	Particle number	Mass	Particle number
Gaseous disk	$8.6 \times 10^9 M_{\odot}$	1.0×10^6	$3.5 \times 10^{10} M_{\odot}$	9.0×10^5
Gaseous halo	$1.0 \times 10^9 M_{\odot}$	4.0×10^5	$1.1 \times 10^{10} M_{\odot}$	3.0×10^5
Dark matter halo	$1.0 \times 10^{12} M_{\odot}$	1.0×10^6	$1.0 \times 10^{12} M_{\odot}$	3.0×10^5
Stellar disk	$3.4 \times 10^{10} M_{\odot}$	1.0×10^6	$2.5 \times 10^{10} M_{\odot}$	3.0×10^5
Bulge stars	$4.3 \times 10^9 M_{\odot}$	1.25×10^5	$9.2 \times 10^9 M_{\odot}$	3.0×10^4

The mass fraction of the dense gas medium is given by

$$f_{\text{dense}} = \min\left(\alpha \frac{n_{\text{H}}}{1.0 \text{ cm}^{-3}}, 1.0\right), \quad (2)$$

where we adopt $\alpha = 0.12$. While the temperature and density of the dense gas medium are assumed to be constant ($T_{\text{dense}} = 50 \text{ K}$ and $n_{\text{H, dense}} = 10^3 \text{ cm}^{-3}$), we estimate the temperature and density of the diffuse gas medium in each gas particle by considering the conservation of the internal energy in each gas particle. This subgrid model allows us to treat dust processes in the diffuse and dense ISM separately according to their respective properties within each gas particle. Further details of the separation treatment of the two-phase ISM are described in Romano et al. (2022a), and the parameters operating the dust processes in the diffuse and dense ISM are described in Aoyama et al. (2020).

Using these models, we simulate Milky Way-like and NGC 628-like galaxies. While the initial condition for the Milky Way-like galaxy is taken from the AGORA project² (Kim et al. 2016), that for the NGC 628-like galaxy is created by DICE³ (Perret 2016). To create the initial condition of the NGC 628-like galaxy, we need the morphological parameters of stellar and gas distributions in NGC 628. Thus, we compute those parameters based on the observationally obtained radial profiles of stars and gas (for the details on creating initial conditions, see Appendix A). Moreover, we set dark matter and gaseous halos, bulge stars, and stellar and gaseous disks in the initial conditions. The properties of these geometries are summarized in Table 1.

We run the Milky Way-like and NGC 628-like galaxy simulations until the simulation time of 10 Gyr when the metallicities in both simulations are consistent with the observed ones (Berg et al. 2015, for NGC 628). Here, we adopt an initial metallicity of $0.0001 Z_{\odot}$, where Z_{\odot} is the solar metallicity ($Z_{\odot} = 0.013$; Asplund et al. 2009), to start our simulations in the condition of the early universe. For the hydrodynamic simulations, we permit the minimum smoothing length to reach $0.1 \epsilon_{\text{grav}}$, where ϵ_{grav} represents the gravitational softening length. The softening lengths of the Milky Way-like and NGC 628-like galaxy simulations are 40 and 50 pc, respectively.

2.2. Post-processing radiative transfer with SKIRT

We employ the state-of-the-art three-dimensional (3D) Monte Carlo radiative transfer code, SKIRT⁴ (Baes et al. 2011; Camps & Baes 2015, 2020), to produce the SEDs and images from UV to millimeter wavelengths. While SKIRT is evolving into a generic radiative transfer code with capabilities to handle many radiative processes relevant to dust and gas media (e.g., Camps

et al. 2021; Gebek et al. 2023; Vander Meulen et al. 2023; Kapoor et al. 2023; Matsumoto et al. 2023), here we consider extinction, emission, scattering, and self-absorption only by dust. We include stochastic heating of dust grains, which is particularly important for small grains and PAHs (Camps et al. 2015). The code is set up to deal with dust mixtures with spatially varying grain size distributions and optical properties⁵. SKIRT has been optimized to post-process snapshots from hydrodynamical galaxy simulations and contains mechanisms to read in SPH, adaptive mesh refinement, and moving-mesh simulations (Saftly et al. 2013, 2014; Camps et al. 2013; Baes & Camps 2015). The methodology to set up SKIRT simulations based on various types of hydrodynamical simulations is described in detail in Camps et al. (2018, 2022), Kapoor et al. (2021), Trčka et al. (2022), and Baes et al. (2024). In the following, we describe the details of the post-processing models of the stellar sources and dust composition used in our SKIRT simulations:

Stellar populations: We utilize the Bruzual & Charlot (2003) templates for single stellar populations with the Chabrier (2003) initial mass function. The intrinsic SED of each star particle is determined based on its stellar age, metallicity, and initial stellar mass. We note that, under the initial conditions of the hydrodynamic simulations, the disk and bulge star particles are pre-assigned to make the galaxy dynamically stable. This means that some stars already exist at the simulation time of $t = 0 \text{ Gyr}$. Thus, we need to construct the star formation history (SFH) before $t = 0 \text{ Gyr}$ for the disk and bulge star particles. Since we run the simulations until $t = 10 \text{ Gyr}$ and assume the galaxy age to be comparable to the cosmic age (13.8 Gyr), the disk and bulge stars have formed between $t = -3.8$ and $t = 0 \text{ Gyr}$. Therefore, in post-processing, we randomly assign their ages to obtain a constant SFH in the 3.8 Gyr interval before $t = 0 \text{ Gyr}$. The metallicity of the disk and bulge star particles is the same as the initial metallicity of $0.0001 Z_{\odot}$.

Dust models: We apply the following dust composition model to each gas particle containing dust grains in the post-processing. First, larger dust grains ($a > 1.3 \text{ nm}$) are designated as silicate and carbonaceous dust grains. The grain size boundary of $a = 1.3 \text{ nm}$ between smaller and larger grains is taken from the definition of the maximum size of PAHs in Draine & Li (2001) and Draine et al. (2007). The mass fractions of silicate and carbonaceous dust (denoted as f_{silicate} and f_{carbon} , respectively) in each gas particle are estimated based on the abundance of Si and C within the gas particle following Hirashita & Murgia (2020) as

$$f_{\text{silicate}} = \frac{6Z_{\text{Si}}}{6Z_{\text{Si}} + Z_{\text{C}}}, \quad (3)$$

$$f_{\text{carbon}} = (1 - f_{\text{silicate}}), \quad (4)$$

⁵ Configuring custom dust mixes is described in https://skirt.ugent.be/root/_tutorial_custom_dust.html

² <https://sites.google.com/site/santacruzcomparisonproject/>

³ <https://bitbucket.org/vperret/dice/src/master/>

⁴ www.skirt.ugent.be.

where Z_{Si} and Z_{C} represent the mass abundances of Si and C within each gas particle, respectively. The factor of 6 is obtained from the mass fraction of Si in silicate, as described in Hirashita & Kuo (2011) and Hirashita & Murga (2020). As shown by Hirashita et al. (2020), our model tends to underpredict PAH emission (see also Chang et al. 2022). To improve our predictions in a maximally acceptable manner within our model framework, we assume that all the smaller grains ($a \leq 1.3$ nm) are carbonaceous. This is consistent with the grain model obtained by Weingartner & Draine (2001) as a result of fitting to the Milky Way extinction curve: in their model, the grain size distribution of silicate has a steeper decline toward small grains while that of carbonaceous dust is enhanced at small radii. As a consequence of this assumption, the grains with $a \leq 1.3$ nm are composed of PAH^0 , PAH^+ , and non-aromatic carbonaceous grains. Since the aromatization and its inverse reaction predominantly occur in the diffuse and dense media, respectively, the mass fractions of aromatic (PAH^0 and PAH^+) carbonaceous grains correspond to the diffuse gas fraction ($f_{\text{aroma}} = 1 - f_{\text{dense}}$; Hirashita & Murga 2020). In the analysis of this paper, the PAH mass fraction is given by

$$q_{\text{PAH}} = \frac{M_{\text{PAH}}(a \leq 1.3 \text{ nm})}{M_{\text{(total dust)}}} \times 100. \quad (5)$$

Finally, to estimate the mass fraction for the PAH^0 and PAH^+ in the aromatic carbonaceous dust grains of each gas particle, we use the ionization fraction from the “standard” ionization model in Draine et al. (2021) and Hensley & Draine (2023):

$$f_{\text{ion}}(a) = 1 - \frac{1}{1 + a/10 \text{ \AA}}. \quad (6)$$

The opacities and calorimetric properties of PAHs, silicate, and carbonaceous grains (assumed to be graphite) follow the prescription of Draine & Li (2007).

Instrument setups of the Milky Way-like galaxy: We observe the galaxy at a distance of 10 Mpc and inclination angles of 0 and 90°. For generating the synthetic observational data, we set the fields of views to $(40 \text{ kpc})^2$ and adopt a pixel size of 50 pc, which is close to the gravitational softening length of the Milky Way-like galaxy simulation. We select pixels of each band data with an intensity ($I_{\nu} > 0.01 \text{ MJy sr}^{-1}$) to avoid pixels with significant Monte Carlo noise in SKIRT.

Instrument setups of the NGC 628-like galaxy: NGC 628 is located at a distance of 9.77 Mpc, and the inclination angle is 8.9° (Leroy et al. 2021). Thus, the simulated galaxy is observed under the same conditions as the actual galaxy. For comparing this simulation with the actual observations in Section 5, we use the fields of views of $(20 \text{ kpc})^2$ and a pixel size of 50 pc, which corresponds to the gravitational softening length of the NGC 628-like galaxy simulation. The pixels of each band data with an intensity ($I_{\nu} > 0.01 \text{ MJy sr}^{-1}$) are selected. When we compare the simulation data with the *Herschel* and *Spitzer* data, the resolutions of the simulation data are reduced to 600 pc to make the consistency of the beam size of the *Herschel* PACS 160 μm for NGC 628 (see also Section 2.3).

2.3. Observational data and analysis

For the observational photometric data of NGC 628, we use the Dustpedia database (Davies et al. 2017; Clark et al. 2018)⁶, the

⁶ <http://dustpedia.astro.noa.gr>

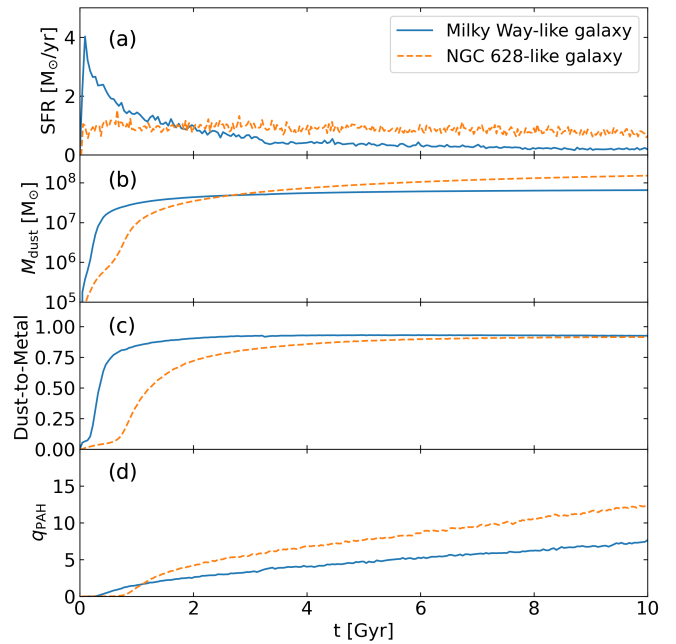


Fig. 1: Time evolution of global physical properties of the Milky Way-like (lines) and NGC 628-like galaxies (blue solid and orange dashed lines, respectively). The evolution of (a) SFR, (b) dust mass, (c) dust-to-metal mass ratio, and (d) PAH mass fraction are shown.

Spitzer Local Volume Legacy survey (Dale et al. 2009), and the PHANGS (Physics at High Angular resolution in Nearby Galaxies) survey (Lee et al. 2023)⁷ for *Herschel*, *Spitzer*, and *JWST* data, respectively. More specifically, we use the *Herschel* PACS 70 and 160 μm bands, the *Spitzer* IRAC 8 μm and MIPS 24 μm bands, and *JWST* MIRI 7.7, 11.3, and 21 μm bands. After we obtain the data, we convolve each image with the kernel function of the point spread function of each instrument. The kernel functions are taken from the Astronomical Convolution-kernel repository (Aniano et al. 2011)⁸. To accomplish the comparison between the observations and the NGC 628-like galaxy simulation in Section 5, we averaged the observational data so that the spatial resolutions of *JWST* images are reduced to 50 pc, which corresponds to the softening length of the simulation. The resolutions of the *Herschel* and *Spitzer* images are unified to 600 pc, which corresponds to the beam size of the *Herschel* PACS 160 μm . After these processes, we select the averaged pixels with a 1 sigma level of the original photometric data.

3. Overall evolution of the galaxy properties of the isolated galaxy simulations

We provide overviews of the simulated galaxies and show the time evolution of global quantities that are important to understand the dust evolution for the Milky Way-like and NGC 628-like cases.

Figure 1(a) shows the SFH of the Milky Way-like and NGC 628-like galaxies. In the Milky Way-like galaxy, a large amount of gas assumed in the galactic center starts to contract, leading to explosive star formation in the early stages of the simulation (hereafter, referred to as the starburst phase). Subsequently, star

⁷ <https://sites.google.com/view/phangs/home/data>

⁸ <https://www.astro.princeton.edu/~draine/Kernels.html>

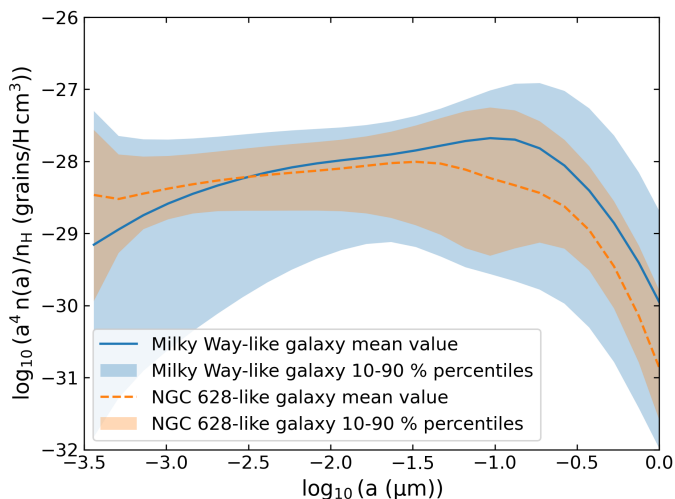


Fig. 2: Grain size distribution in the Milky Way-like (blue solid line) and NGC 628-like (orange dashed line) galaxies at $t = 10$ Gyr. The solid lines and the shades show the mean values and the range of 10th–90th percentiles for the sample of gas particles, respectively.

formation and its feedback gradually deplete the gas in the center of the galaxy, resulting in a decrease in the SFR. In contrast, star formation occurs moderately in the NGC 628-like galaxy, since the gas radial profile of the NGC 628-like galaxy is flat and not dense enough to cause explosive star formation. Thus, the gas is slowly consumed by star formation with $\text{SFR} = 1.0 M_{\odot} \text{ yr}^{-1}$ over 10 Gyr.

The different SFHs between the Milky Way-like and NGC 628-like galaxies lead to their different dust evolution. The total dust mass increases more rapidly for the Milky Way-like galaxy at $t < 1.0$ Gyr than for the NGC 628-like galaxy, as shown in Fig. 1(b) since more dust is produced in the starburst phase of the Milky Way-like galaxy.

The dust-to-metal mass ratio gives us insights into the efficiency of dust accretion in the ISM since dust grains grow by acquiring gas-phase metals (e.g., Hirashita 1999; Chiang et al. 2018). Figure 1(c) shows that the dust-to-metal mass ratio of the Milky Way-like galaxy increases more steeply than that of the NGC 628-like galaxy since the quicker metal enrichment in the starburst phase of the Milky Way-like galaxy leads to more efficient accretion of gas-phase metals onto dust grains.

Figure 1(d) shows the evolution of the PAH mass fractions, which indicates the efficiency of shattering since PAHs represent small grains. The PAH mass fraction in the Milky Way-like galaxy less steeply increases since the Milky Way-like galaxy contains more amounts of dense gas than the NGC 628-like galaxy, and hence, shattering is less efficient. The difference in the ISM conditions between these galaxies also reflects their grain size distributions at $t = 10$ Gyr as shown in Fig. 2. The mean grain size distributions have different slopes between the two simulations in such a way that the Milky Way-like galaxy (blue solid line) is more dominated by large grains than the NGC 628-like galaxy (orange dashed line). At $t = 10$ Gyr, the shape is determined by the balance between coagulation and shattering. Coagulation turns more small grains into large grains in the Milky Way-like galaxy, since the galaxy contains more amounts of dense gas than the NGC 628-like galaxy. These results suggest that different ISM conditions and SFHs cause different dust evolution.

4. Observational signatures of the grain size evolution in the Milky Way-like galaxy

To investigate observational signatures of the dust size evolution, we focus on the results from the Milky Way-like galaxy simulations. We note that the following discussion in this section does not significantly change even if we involve the results of the NGC 628-like galaxy simulation. Also, to scrutinize the ISM processes across the whole galaxy with minimal interference from dust extinction, we use the synthetic observation data of a face-on view of the Milky Way-like galaxy in Section 4.2.

4.1. Influences of the dust size evolution on dust emission

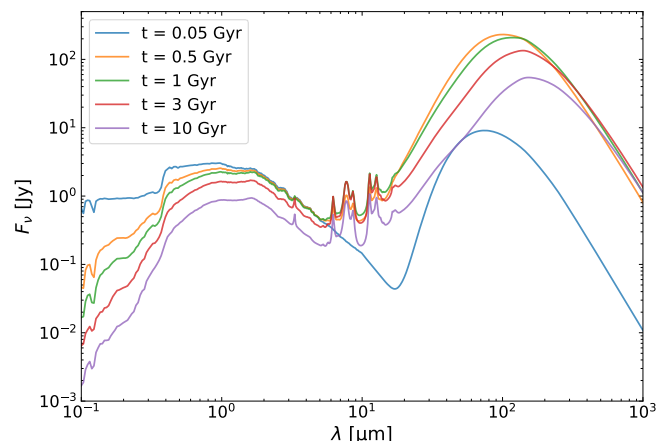


Fig. 3: Evolution of the global SED for the Milky Way-like galaxy simulation. The different colored lines correspond to the total SEDs at $t = 0.05, 0.5, 1, 3,$ and 10 Gyr (cyan, orange, green, red, and purple lines, respectively). The observed flux density is estimated at a distance of 10 Mpc.

We investigate how dust evolution is reflected in SEDs at various stages of galaxy evolution. Figure 3 shows the total SEDs of the Milky Way-like galaxy simulation at $t = 0.05, 0.5, 1, 3,$ and 10 Gyr. At $t = 0.05$ Gyr, only emission of large dust grains can be observed around $\lambda = 70 \mu\text{m}$, as dust production is dominated by stellar sources, which predominantly produce large grains. At $t \geq 0.5$ Gyr, emission from small dust grains and PAHs become noticeable around $\lambda = 10 \mu\text{m}$. This is due to shattering, which acts as a source of small grains, and accretion, which increases the abundance of small grains (see also Asano et al. 2013; Hirashita & Aoyama 2019). Given the monotonic decrease in the SFR in the Milky Way-like galaxy at later epochs, the intrinsic radiation from young stars at UV to optical wavelengths is weakened with time. Consequently, the peak of dust emission in the SED shifts from $\lambda = 70$ to $150 \mu\text{m}$ over time. This shift corresponds to a decrease in dust temperature from $T_{\text{dust}} = 40$ to 20 K. On the other hand, the dust mass monotonically increases with time in the Milky Way-like galaxy through mainly the accretion of gas-phase metals. Thus, at $t = 1$ Gyr, the total IR luminosity achieves its maximum.

Figure 4 shows stellar and dust emission maps from the Milky Way-like galaxy simulation at the simulation times of $t = 0.05, 0.5, 1.0, 3.0,$ and 10 Gyr. The first two rows show stellar emission with colors synthesized using the SDSS i (red), r (green), and g (blue) fluxes and the GALEX FUV flux (additionally enhanced blue color) as seen from face-on and edge-on. As viewed face-on, old stars radiate throughout the entire galaxy

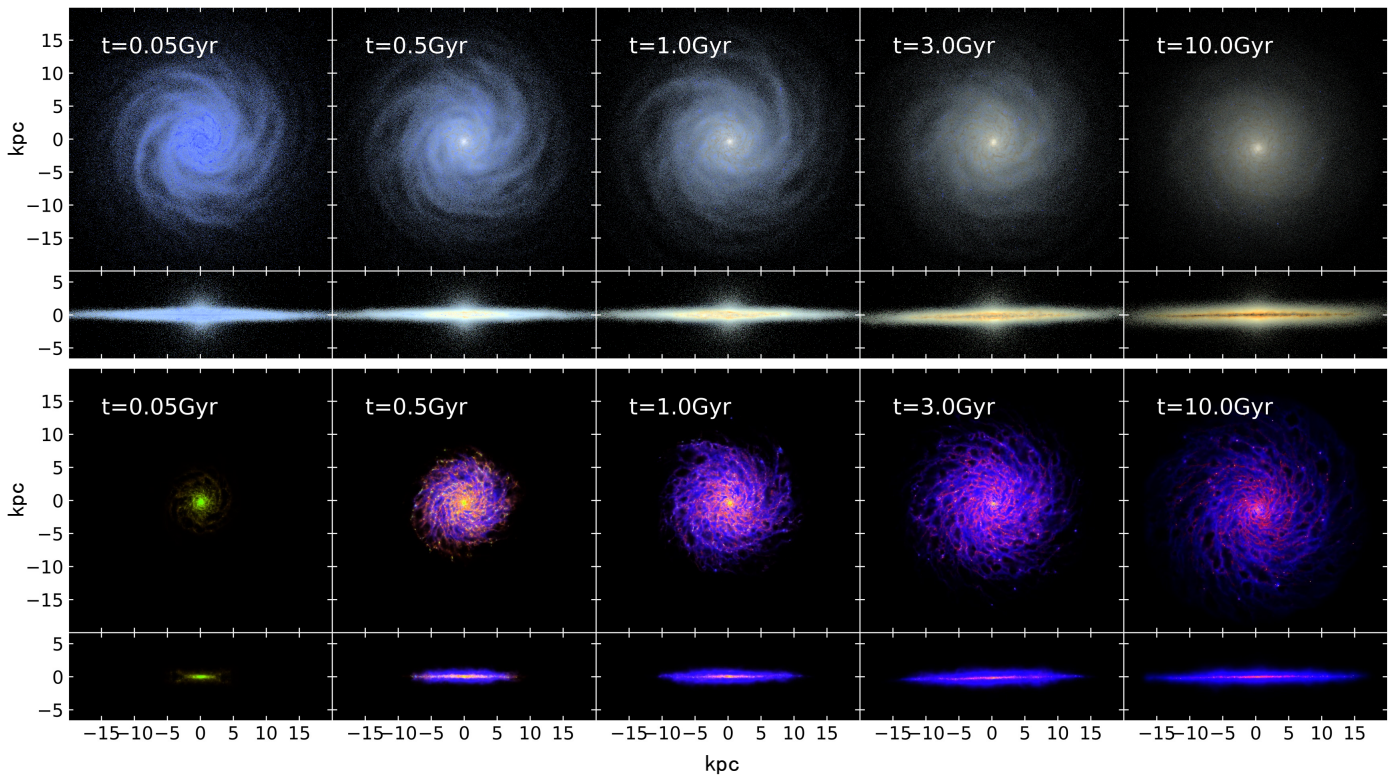


Fig. 4: Evolution of stellar (first and second rows) and dust emission maps (third and fourth rows) of the Milky Way-like galaxy simulation. The panels show the emission maps at $t = 0.05, 0.5, 1, 3,$ and 10 Gyr from left to right. The images on the first and third (second and fourth) rows are face-on (edge-on) views. The stellar emission maps consist of the SDSS i (red), r (green), and g (blue) fluxes with an additionally enhanced blue level for the *GALEX* FUV flux. The dust emission maps are synthesized by the *Spitzer* IRAC $8\ \mu\text{m}$ (blue), *Herschel* PACS $70\ \mu\text{m}$ (green), and *Herschel* PACS $160\ \mu\text{m}$ (red) fluxes.

(appearing in white), while UV radiation from young stars (blue) originates from star-forming regions, which tend to be concentrated in dense clumps along the spiral arms. As viewed face-on and edge-on, the effect of dust attenuation is prominent at later stages of the galaxy evolution when dust formation has proceeded enough to shield the stellar radiation. Spiral-shaped and horizontally extended dark lanes in the stellar emission develop from face-on and edge-on views, respectively.

The bottom two rows of Fig. 4 show the dust emission maps consisting of *Spitzer* IRAC $8\ \mu\text{m}$ (red), *Herschel* PACS $70\ \mu\text{m}$ (green), and *Herschel* PACS $160\ \mu\text{m}$ (blue) fluxes as seen from face-on and edge-on. The IRAC $8\ \mu\text{m}$ band mainly traces the emission from PAHs heated by radiation from young stars, while the PACS $70\ \mu\text{m}$ and PACS $160\ \mu\text{m}$ bands trace emission from warm and cold large dust grains, respectively. At $t = 0.05$ Gyr, large grains are produced by stars in the central region of the galaxy, and the emission from the warm large grains heated by young stars is prominent. At $t \geq 0.5$ Gyr, large dust grains are produced by stars in the spiral arms, and simultaneously accretion and shattering become prevalent in the dense and diffuse ISM, respectively. These processes increase small grains, leading to significant emission from small dust grains and PAHs in the MIR (i.e., the color becomes bluer in the images). At $t \geq 1$ Gyr, coagulation also becomes efficient in the dense ISM, enhancing emission from large dust grains in the central regions and spiral arms of the galaxy. The emission from small dust grains and PAHs is prominent in diffuse regions along the spiral arms. At later times, as star formation activity declines, the overall dust emission becomes weaker, and the color becomes redder because of lower dust temperature. Finally, at $t = 10$

Gyr, the functional shape of the grain size distribution at each region converges to the one determined by the balance between the shattering and coagulation rates (see also Fig. 2). Since the overall density is higher in the central regions (thus, coagulation is more enhanced), the emission from large and small grains is relatively prominent in the inner and outer regions of the galaxy, respectively.

4.2. Indicator of the PAH mass fraction

We investigate promising indicators of PAH mass fractions in the ISM using multi-wavelength intensity ratios in the SKIRT simulation of the Milky Way-like galaxy. The validity of the adopted ratios as a good indicator is tested against actual PAH mass fractions of the Milky Way-like galaxy simulation. Since the PAH emission is the most prominent in the $8\ \mu\text{m}$ band among the bands available for *Spitzer* and *JWST*, we construct the indicators by combining the $8\ \mu\text{m}$ band and other wavelengths. We focus on the following two: one is the intensity ratio using representative MIR bands, that is, the 8 to $24\ \mu\text{m}$ intensity ratio, $I_\nu(8\ \mu\text{m})/I_\nu(24\ \mu\text{m})$, and the other is the $8\ \mu\text{m}$ to the total infrared intensity ratio, $\nu I_\nu(8\ \mu\text{m})/I_{\text{TIR}}$. Here we denote the intensity per frequency at wavelength λ as $I_\nu(\lambda)$. Also, we note that we investigate those indicators with the spatially resolved information of the 50 -pc pixel data constructed in Section 2.2.

4.2.1. $I_\nu(8\ \mu\text{m})/I_\nu(24\ \mu\text{m})$

Figure 5 shows the pixel-based relation between PAH mass fraction of q_{PAH} and $I_\nu(8\ \mu\text{m})/I_\nu(24\ \mu\text{m})$ at $t = 0.5, 1.0, 3.0,$

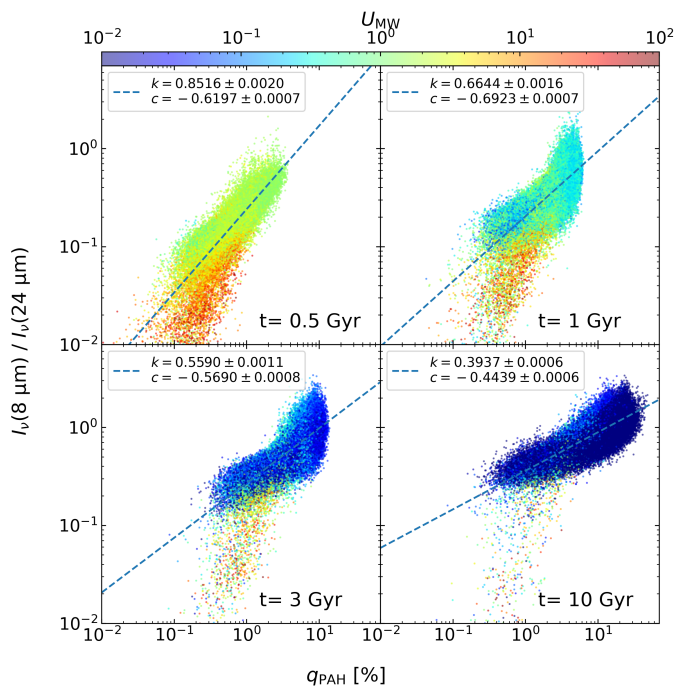


Fig. 5: Pixel-based relation between the 8-to-24 μm intensity ratio and the PAH mass fraction of the Milky Way-like galaxy simulation at $t = 0.5, 1.0, 3.0,$ and 10 Gyr from top left to bottom right. The color represents density-weighted mean intensity at 1000 \AA relative to the Milky Way value as shown by the color bar on the top of each panel. Blue dashed lines indicate the best-fit relation given by Eq. (7), and the legends show the values of coefficients k and c .

and 10 Gyr. To investigate the effect of the radiation field (or dust heating), we color-code the data points with the density-weighted mean intensity at 1000 \AA relative to the Milky Way value of $10^6 \text{ photons cm}^{-2} \text{ s}^{-1} \text{ eV}^{-1}$, U_{MW} . We fit the data at each time by the following equation:

$$\log_{10}(\text{Intensity Ratio}) = k \log_{10}(q_{\text{PAH}}) + c, \quad (7)$$

where k and c are coefficients derived from the fitting, and k is associated with the radiative processes of dust grains. The best-fit relation at each time is indicated as blue dashed lines in Fig. 5. We find that $I_{\nu}(8 \mu\text{m})/I_{\nu}(24 \mu\text{m})$ correlates with q_{PAH} at each time. The $8 \mu\text{m}$ band is almost purely dominated by the PAH emission, while the $24 \mu\text{m}$ band is contaminated by emission from larger dust grains with $a \gtrsim 20 \text{ \AA}$ (Draine & Li 2007), so that $I_{\nu}(8 \mu\text{m})/I_{\nu}(24 \mu\text{m})$ increases with q_{PAH} . However, we also find that stronger radiation fields decrease the ratio at a fixed q_{PAH} , as color indicates. This is because stronger radiation fields cause higher dust temperatures, shifting the large grain emission toward shorter wavelengths and raising emission at $24 \mu\text{m}$ (Draine & Li 2007; Schreiber et al. 2018). Consequently, given the monotonic decrease in SFR with time in the Milky Way-like galaxy, the best-fitting slope becomes shallower with time. The above dependence on the radiation field, however, is not strong enough to break the correlation between $I_{\nu}(8 \mu\text{m})/I_{\nu}(24 \mu\text{m})$ and q_{PAH} at each time. Therefore, $I_{\nu}(8 \mu\text{m})/I_{\nu}(24 \mu\text{m})$ can be an indicator of the PAH mass fraction with a tendency of underestimating the PAH mass fraction in regions of strong radiation fields such as star-forming regions. In particular, $I_{\nu}(8 \mu\text{m})/I_{\nu}(24 \mu\text{m})$ has the advantage of using only two bands in the MIR, which is useful if the available wavelength coverage is limited. We note

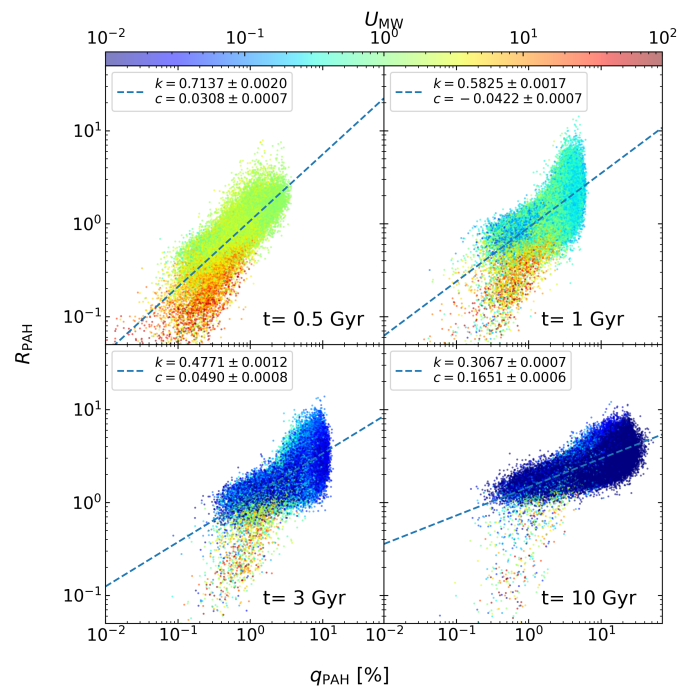


Fig. 6: Same as Fig. 5 but for R_{PAH} .

that the above results are also applicable to an indicator of PAH mass fraction, R_{PAH} , for *JWST* as shown in Fig. 6.

4.2.2. $\nu I_{\nu}(8 \mu\text{m})/I_{\text{TIR}}$

Here, we use the total infrared intensity estimated by the following equation:

$$I_{\text{TIR}} = 0.95 \nu I_{\nu}(8 \mu\text{m}) + 1.15 \nu I_{\nu}(24 \mu\text{m}) + \nu I_{\nu}(70 \mu\text{m}) + \nu I_{\nu}(160 \mu\text{m}), \quad (8)$$

which is suggested by Draine & Li (2007). They theoretically indicate that the estimated total infrared intensity differs from the actual one within the relative difference of 10 % for the radiation fields of $0.1 < U_{\text{MW}} < 10^2$. Here, we expect to maintain higher spatial resolutions of the observed data by utilizing the estimation with bands at up to $160 \mu\text{m}$ although there are other estimation methods with longer wavelength bands for the total infrared intensity (Boquien et al. 2011; Galametz et al. 2013). Figure 7 shows the pixel-based relation between PAH mass fraction and $\nu I_{\nu}(8 \mu\text{m})/I_{\text{TIR}}$ at $t = 0.5, 1.0, 3.0,$ and 10 Gyr. The color represents the density-weighted mean intensity at 1000 \AA relative to the Milky Way value, U_{MW} . We find that the ratio tightly correlates with q_{PAH} and is not affected by the local radiation field of U_{MW} unlike $I_{\nu}(8 \mu\text{m})/I_{\nu}(24 \mu\text{m})$. Remarkably, the parameters of the best-fit relation (blue) are consistent among the different times within the relative difference of 5%. This is because both total and $8 \mu\text{m}$ intensities are proportional to the strength of the local radiation field (Draine & Li 2007), and hence, the effect of the radiation field is canceled out. Additionally, we perform linear regression for all of the data including snapshots at different times. We find that the PAH mass fraction of q_{PAH} can be formulated by the following equation,

$$q_{\text{PAH}} = 66 \left(\frac{\nu I_{\nu}(8 \mu\text{m})}{I_{\text{TIR}}} \right)^{1.2}. \quad (9)$$

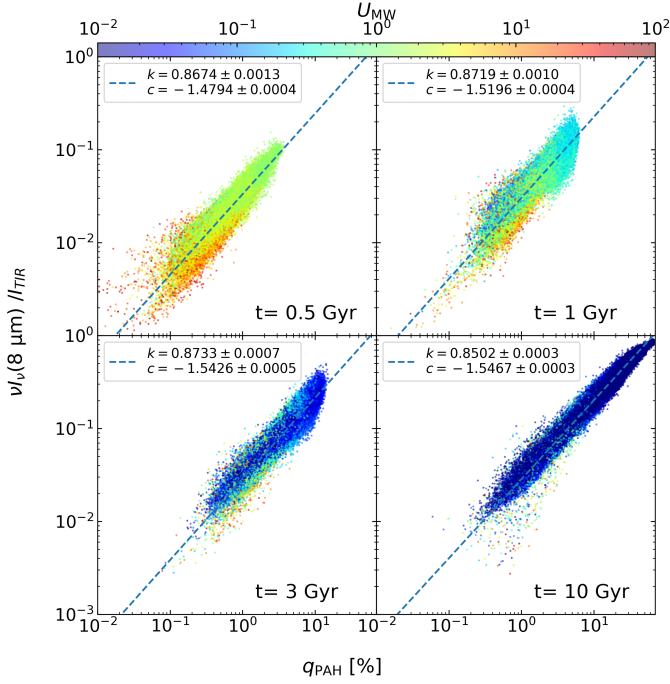


Fig. 7: Pixel-based relation between the $8\ \mu\text{m}$ -to-total IR intensity ratio and the PAH mass fraction of the Milky Way-like galaxy simulation at $t = 0.5, 1.0, 3.0,$ and $10\ \text{Gyr}$ from top left to bottom right. The color represents the density-weighted mean intensity at $1000\ \text{\AA}$ relative to the Milky Way value as indicated by the color bar at the top of each panel. Blue dashed lines indicate the best-fit relation of Eq. (7).

Therefore, we suggest that $\nu I_\nu(8\ \mu\text{m})/I_{\text{TIR}}$ is a good indicator of the PAH mass fraction in the ISM of galaxies in various stages of galaxy evolution.

4.2.3. Dependence of the PAH mass fraction on the metallicity and hydrogen surface density

To demonstrate the usefulness of $\nu I_\nu(8\ \mu\text{m})/I_{\text{TIR}}$ as an indicator of the PAH mass fraction, we investigate the spatially resolved relation among the PAH mass fraction, gas-phase metallicity, and hydrogen surface density. Appendix B shows the projected maps of PAH mass fraction, metallicity, and hydrogen surface density. Figure 8 shows the pixel-based relation between $\nu I_\nu(8\ \mu\text{m})/I_{\text{TIR}}$ and metallicity at $t = 0.5, 1.0, 3.0,$ and $10\ \text{Gyr}$. The color represents the hydrogen surface density of each pixel. The purple star symbols represent the global intensity ratio and metallicity of the galaxy at four epochs, and the dashed lines indicate the time evolution of global properties over the epochs (from the lower left to the upper right in each panel). We find that the global $\nu I_\nu(8\ \mu\text{m})/I_{\text{TIR}}$ (PAH mass fraction) increases with time and metallicity. This global trend is also suggested by observations using many galaxy samples (Galliano et al. 2008a; Rémy-Ruyer et al. 2015; Shim et al. 2023). Shattering and accretion happen in separate ISM phases, and their interplay increases small grains (and PAHs) on a galactic scale in our simulations (Hirashita 2012). Hence, the global PAH mass fraction evolves with metallicity.

In the pixel-based analysis, the local PAH mass fraction is associated with the local ISM conditions such as metallicity and hydrogen surface density. At $t = 0.5\ \text{Gyr}$, $\nu I_\nu(8\ \mu\text{m})/I_{\text{TIR}}$ increases with metallicity in a lower metallicity regime ($Z \lesssim$

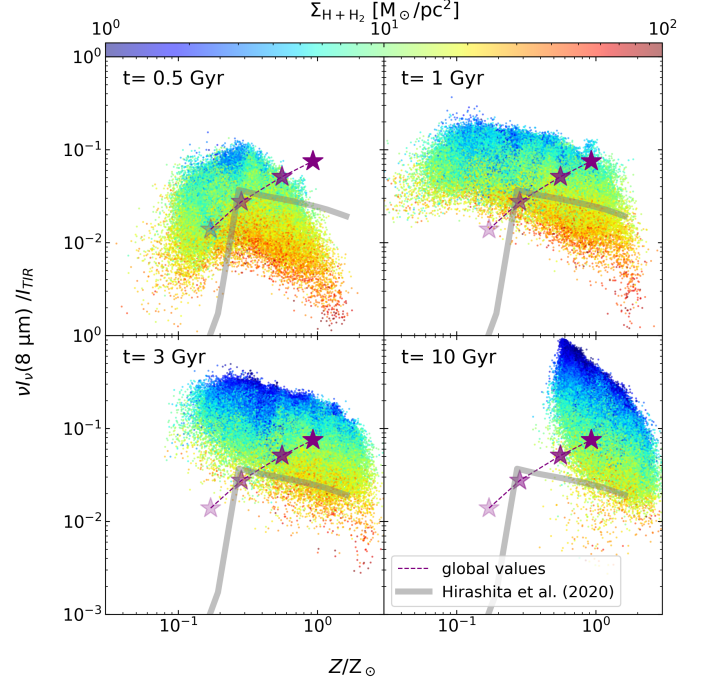


Fig. 8: Time evolution of pixel-based relation among the $8\ \mu\text{m}$ -to-total IR intensity ratio, gas-phase metallicity, and hydrogen surface density for the Milky Way-like galaxy simulation. The panels show the relation at $t = 0.5, 1.0, 3.0,$ and $10\ \text{Gyr}$ from top left to bottom right. The color bar indicates the hydrogen surface density of each pixel. In each panel, the time evolution of the entire distribution over the four epochs is also indicated by the purple dashed lines. The purple star symbols represent the global intensity ratio and metallicity of the galaxy at $t = 0.5, 1.0, 3.0,$ and $10\ \text{Gyr}$ from the lower left to the upper right in each panel (the symbol transparency decreases) and are connected by the dashed line. We note that the intensity ratio and metallicity are the intensity- and mass-weighted values, respectively. The grey line shows the evolutionary path in the one-zone dust evolution model by Hirashita & Murga (2020) under the condition of $f_{\text{dense}} = 0.5$, $\tau_{\text{SF}} = 5\ \text{Gyr}$, and $U_{\text{MW}} = 1$.

$0.2 Z_\odot$) while it decreases with metallicity in a higher metallicity regime ($Z \gtrsim 0.2 Z_\odot$), as suggested by a one-zone dust evolution model (grey line; Hirashita & Murga 2020). We note that the number of pixels in the lower metallicity regime is significantly reduced by the pixel selection because those with significant noises are excluded in our analysis in Section 2.3. At low metallicity, the interplay between accretion and shattering increases the PAH mass fraction, producing a trend of increasing the PAH mass fraction with metallicity. At higher metallicity, dust grows sufficiently through metal accretion, and the effect of coagulation becomes prominent. The coagulation turns small grains, including PAHs, into larger grains and plays an important role in decreasing the PAH mass fraction at a high-metallicity regime. At $\geq 1.0\ \text{Gyr}$, $\nu I_\nu(8\ \mu\text{m})/I_{\text{TIR}}$ anticorrelates with metallicity since most of the regions reach high metallicity. We also find that $\nu I_\nu(8\ \mu\text{m})/I_{\text{TIR}}$ depends on the hydrogen surface density since coagulation converts small grains, including PAHs, to larger grains in the dense ISM.

These results are roughly consistent with observational studies. Egorov et al. (2023) report a weak anti-correlation between R_{PAH} and oxygen abundance based on the spatially resolved observations of four galaxies with high metallicity ($12+\log(\text{O}/\text{H}) \gtrsim 8.4$). Chasten et al. (2023a) show a tendency

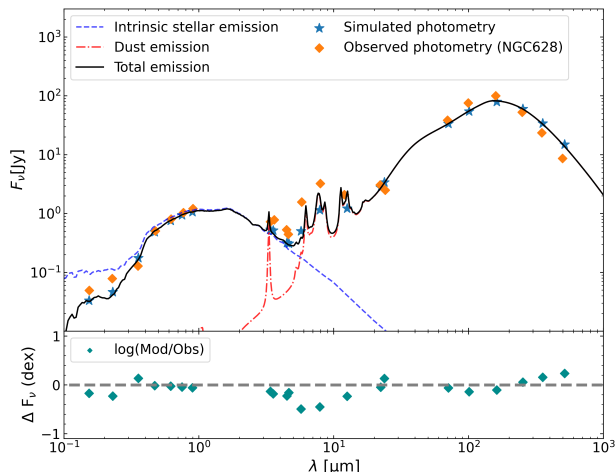


Fig. 9: Comparison of the global SED between the NGC 628-like galaxy simulation and actual observations. *Upper panel:* The black solid line shows the global SED of the NGC 628-like galaxy simulation at $t = 10$ Gyr. Blue dashed and red dash-dotted lines represent the intrinsic stellar and dust emission, respectively. The orange and blue diamonds correspond to the simulated and observed photometries of the total SEDs (Relaño et al. 2020), respectively. *Lower panel:* Difference in the photometries between the simulation and observation data.

to increase R_{PAH} with oxygen abundance at low oxygen abundance ($12 + \log(\text{O}/\text{H}) \lesssim 8.5$) but flatten out at high oxygen abundance ($12 + \log(\text{O}/\text{H}) \gtrsim 8.5$). However, those observations cover only four galaxies, and future observations are necessary to verify whether there are general trends for the spatially resolved PAH mass fractions to increase and decrease with metallicity at a lower and higher metallicity, respectively.

Therefore, the spatially resolved relation of the PAH mass fraction against metallicity is related to the efficiency of coagulation, shattering, and accretion across diverse ISM conditions, and the analysis of the spatially resolved relation leads us to interpret dust evolution in observations.

5. NGC 628-like galaxy simulation

NGC 628 is an ideal galaxy to validate our dust model based on spatially resolved data since it is well-observed with a high spatial resolution in the PHANGS surveys (Kennicutt et al. 2011; Leroy et al. 2021; Lee et al. 2023). Here, we model the NGC 628-like galaxy simulation according to the morphological parameters of the NGC 628 (see Appendix A) to make a fair comparison. We use the simulation snapshot at $t = 10$ Gyr as a representative age of present-day galaxies. More comprehensive comparisons including other nearby galaxies will be presented in our future work (van der Giessen et al. in preparation).

5.1. SED comparisons

Figure 9 shows the total SED comparison between the simulation and the actual observations of NGC 628 (Relaño et al. 2020, blue and orange diamonds, respectively). The total, intrinsic stellar, and dust emission SEDs of the NGC 628-like simulation are also indicated by black solid, blue dashed, and red dash-dotted lines, respectively. The lower panel indicates the difference in

the photometries between the simulation and the observations. Stellar emission at optical and near-IR wavelengths of the simulated galaxy is consistent with that of the observations while the emission at UV wavelengths in the simulation is weaker than that of the observations. This is because the SFR of the simulated galaxy at $t = 10$ Gyr ($\dot{M}_* = 0.75 M_{\odot} \text{ yr}^{-1}$) is lower than that reported by the observation ($\dot{M}_* = 1.7 M_{\odot} \text{ yr}^{-1}$) (Leroy et al. 2021). On the other hand, dust emission at longer wavelengths of $\lambda \geq 20 \mu\text{m}$ in the simulation is consistent with that in observations while the PAH emission at MIR wavelengths in the simulation is lower than that in observations by about 0.5 dex. This result implies that our dust model underestimates the PAH mass, as reported in Hirashita et al. (2020) and Hirashita (2023). To explore where the PAH mass fraction is underestimated in our simulation, we perform the pixel-based comparison of the PAH mass fraction in the next section.

5.2. Spatial comparison of PAH mass fraction

We compare the spatially resolved data of $\nu I_{\nu}(8 \mu\text{m})/I_{\text{TIR}}$ between our simulation and *Herschel/Spitzer* observations. The observations cover large scales up to the galactic radius of $r \sim 10$ kpc, but the spatial resolution is about 600 pc. Figure 10(a) shows the comparison of the relation between $\nu I_{\nu}(8 \mu\text{m})/I_{\text{TIR}}$ and the intensity at $160 \mu\text{m}$. The line and shaded area correspond to the median value and the range between the 10th and 90th percentiles, respectively. Here, the $160 \mu\text{m}$ band traces large grains in radiative equilibrium and represents the dust mass distribution. We find that $\nu I_{\nu}(8 \mu\text{m})/I_{\text{TIR}}$ from the simulation is lower than that of the observation in the entire range of $160 \mu\text{m}$. This indicates an underestimation of the PAH mass fraction in our model, regardless of location. To estimate how much additional PAH mass is required in the NGC 628-like galaxy simulation (hereafter, referred to as fiducial model), we assume eight times the PAH mass of the fiducial model and find $\nu I_{\nu}(8 \mu\text{m})/I_{\text{TIR}}$ can be consistent with that of the observation. Therefore, we conclude that we underestimate the PAH mass abundance by a factor of eight on average in our simulated area.

Furthermore, we compare the spatially resolved data from our simulation and the *JWST* observations (Lee et al. 2023), which has 12 times higher spatial resolution than the *Herschel* observations (a pixel size ~ 50 pc). Here, instead of $I_{\nu}(8 \mu\text{m})/I_{\nu}(24 \mu\text{m})$, we use the intensity ratio of R_{PAH} (Eq. (1)). Fig. 10(b) shows the comparison of R_{PAH} to the intensity at $21 \mu\text{m}$ between our simulation (orange) and the observation (blue). We find that, in both simulation and observation, R_{PAH} decreases as the $21 \mu\text{m}$ intensity increases. This trend can be explained by our model in which coagulation is more efficient in denser regions with higher $21 \mu\text{m}$ intensities. Figures 11(a) and (b) show the intensity maps at $21 \mu\text{m}$ of the entire NGC 628-like galaxy at $t = 10$ Gyr and the central 6 kpc regions of the galaxy, respectively. Figs. 11(c) and (d) show the R_{PAH} maps of the entire NGC 628-like galaxy at $t = 10$ Gyr and the central 6 kpc regions of the galaxy, respectively. In Fig. 11(c), R_{PAH} gradually increases toward the outer regions of the galaxy, since shattering is more dominant in the diffuse ISM than coagulation. In the central region of the galaxy (Fig. 11(d)), R_{PAH} is lower in the spiral arms and clumps, where the intensity at $21 \mu\text{m}$ is higher. This is because coagulation is dominant in the dense ISM. These trends are consistent with the results revealed by recent *JWST* observations. Figs. 11(e) and (f) show the observed maps of $21 \mu\text{m}$ intensity and R_{PAH} maps, respectively (Lee et al. 2023). These observations also indicate that R_{PAH} is lower in the spiral arms and clumps, where the $21 \mu\text{m}$ intensity is higher. Alternatively,

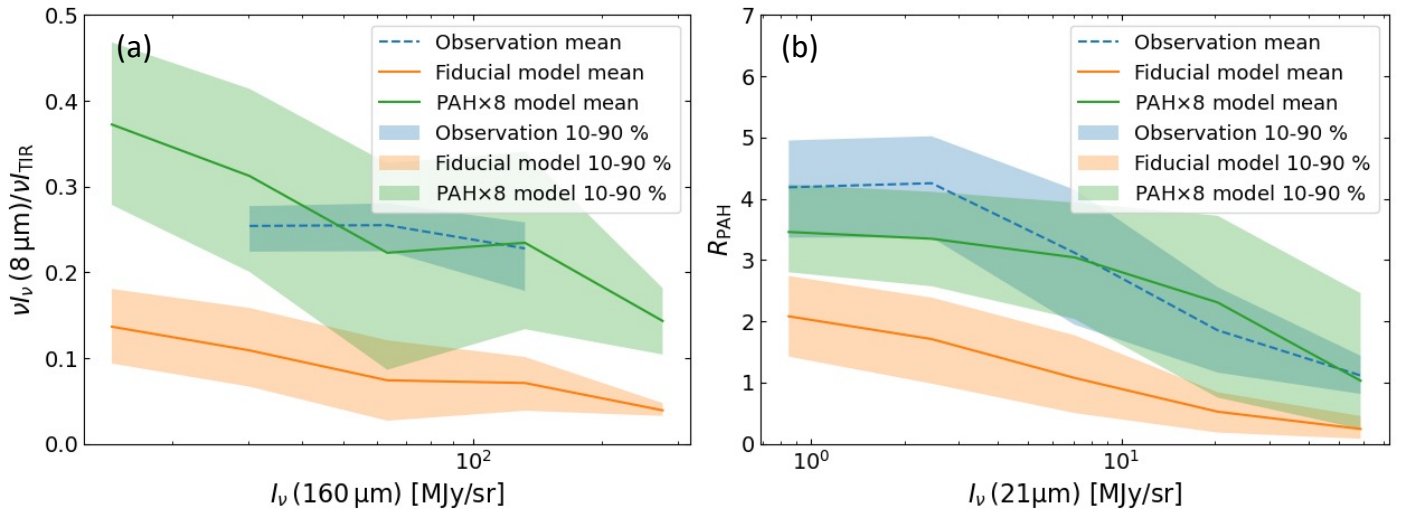


Fig. 10: Pixel-based comparison of the indicators of the PAH mass fraction between the NGC 628-like galaxy simulation and actual observations. *Panel (a):* $\nu I_\nu(8\ \mu\text{m})/I_{\text{TIR}}$ versus the $160\ \mu\text{m}$ intensity for the NGC 628-like galaxy simulation at $t = 10$ Gyr (orange) and based on the *Herschel* and *Spitzer* observations for NGC 628 (blue). *Panel (b):* R_{PAH} versus the $21\ \mu\text{m}$ intensity for the NGC 628-like galaxy simulation at $t = 10$ Gyr (orange) and based on the *JWST* observations for NGC 628 (blue). In both panels, the green color represents the model, in which the PAH mass is enhanced by a factor of eight. The solid and dashed lines represent the mean value over all pixels of the photometric data of the models and observations, and the shaded area corresponds to the 10th–90th percentile range, respectively.

it is also possible that PAHs are destroyed by UV radiation from young stars in star-forming regions in the dense ISM, as discussed in the literature (e.g., Egorov et al. 2023; Chasten et al. 2023b) since $21\ \mu\text{m}$ intensity is expected to increase as UV radiation field becomes stronger. Thus, to discriminate these scenarios, we have to implement PAH destruction due to UV radiation from young stars in future simulations (e.g., Nanni et al. 2023). We also find that the value of R_{PAH} from the simulation is lower than that from the observation, as discussed above: R_{PAH} of the model with the PAH mass enhanced by a factor of eight is consistent with that of the observations, implying that further enhancement of small dust grains in our model is required.

5.3. Insights into additional PAH formation mechanisms

As we discussed above, our dust evolution model underestimates the PAH mass fraction in the entire galaxy, and thus, additional mechanisms to enhance the PAH production in our model are required. In our model, we assume that the main driver of PAH formation is the shattering of large carbonaceous grains, but PAH formation in the envelopes of carbon-rich AGB stars may also be considered. Furthermore, in our model, PAHs might be too destroyed by coagulation in dense ISM. Here, we discuss the possible scenarios to enhance PAHs in the ISM of our simulations.

Cherchneff et al. (1992) suggest that the stellar envelopes of carbon-rich AGB stars can be a site of the PAH formation. Indeed, many observational studies reveal evidence of the PAH formation in the stellar envelopes of AGB stars by identifying the PAH features in the spectra of the individual stars in the Magellanic clouds and our Galaxy (Sloan et al. 2007, 2014; Matsuura et al. 2014). However, some studies based on the Magellanic clouds report that the presence of PAHs in the ISM can not be explained entirely only by carbon-rich AGB stars (Matsuura et al. 2013; Sandstrom et al. 2010; Chasten et al. 2019). Moreover, since NGC 628 has higher metallicity than the Magellanic Clouds, stellar dust production containing PAHs should be even less efficient than dust growth by accretion in the ISM in NGC

628. Thus, it is not probable that stellar PAH production is dominant over PAH formation in the ISM in NGC 628.

In our model, coagulation in the dense ISM efficiently depletes PAHs by converting small grains to larger grains. Hirashita (2023) model a process that prevents small carbonaceous grains from being lost through coagulation by hypothesizing that small carbonaceous grains are not involved in interstellar processing. They succeed in enhancing small grains, especially PAHs, and reproduce the observed global dust SED with the PAH emission at the MIR wavelengths. Although the chemical or physical processes underlying their hypothesis have yet to be justified, their success indicates that a key to the PAH deficiency problem in our model lies in the treatment of interstellar processing of PAHs.

6. Conclusion

In this paper, we aim to investigate how dust evolution is reflected on IR spectral features and provide observational signatures of the dust size evolution in ISM, in particular exploring indicators of PAH mass fraction. We model the dust evolution for two simulations representing star-forming galaxies similar to the Milky Way and NGC 628 using GADGET4-OSAKA (Romano et al. 2022a). We simulate the evolution of grain size distribution in a manner consistent with the physical conditions of the ISM (see Section 2.1) by taking into account interstellar dust processes including stellar dust production, SN destruction, shattering, coagulation, and metal accretion. Furthermore, we separate the dust compositions into silicate and carbonaceous dust grains, and PAHs in post-processing. Then, we perform radiative transfer calculations with SKIRT under the dust optical properties consistent with the grain size distribution and grain composition of the hydrodynamic simulations (see Section 2.2).

We summarize the results as follows:

1. We show the history of dust evolution and star formation for the Milky Way-like and NGC 628-like galaxy simulations (see Fig. 1). The Milky Way-like galaxy shows more rapid

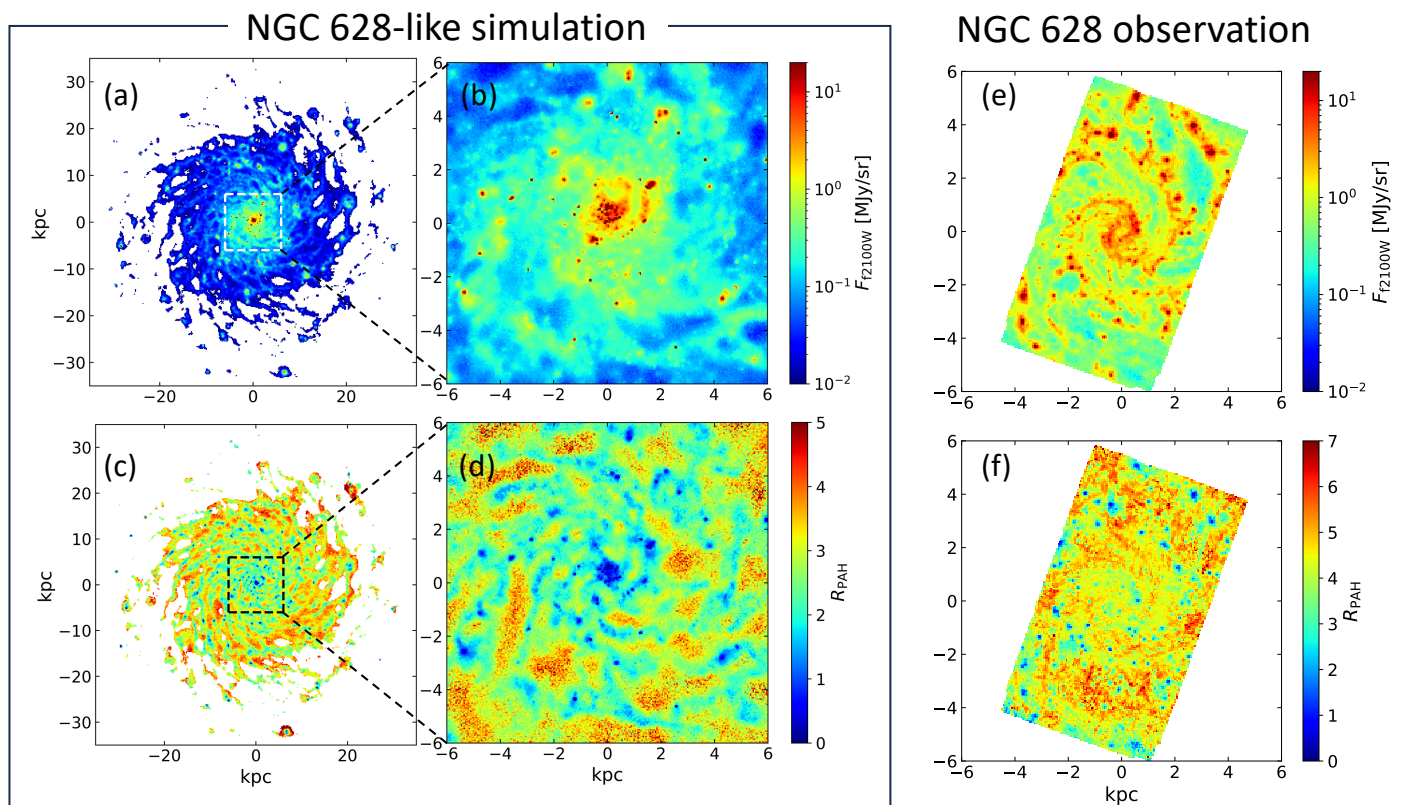


Fig. 11: Comparison of $21\ \mu\text{m}$ intensity and R_{PAH} maps between the NGC 628-like galaxy simulation and *JWST* observations. *Panels (a) and (b):* $21\ \mu\text{m}$ intensity maps of the NGC 628-like galaxy simulation at 10 Gyr on 100 and 20 kpc scales, respectively. *Panels (c) and (d):* R_{PAH} maps of the simulation on 100 and 20 kpc scales, respectively. *Panels (e) and (f):* maps of the $21\ \mu\text{m}$ intensity and R_{PAH} based on the *JWST*/MIRI observations for NGC 628 (Lee et al. 2023), where the spatial resolutions are reduced to 50 pc.

dust formation because of the earlier starburst and metal production than the NGC 628-like galaxy. However, the Milky Way-like galaxy shows less PAH formation in the ISM since the Milky Way-like galaxy contains a large amount of dense gas, where shattering is inefficient. These results suggest that different ISM conditions and SFHs cause different dust evolution and PAH mass fractions among galaxies.

2. We investigate the detailed time evolution of the observable properties for the Milky Way-like simulation. In the early phase, only the emission of large dust grains can be observed around $\lambda = 70\ \mu\text{m}$ in the SED, as dust production is dominated by stellar sources (see Fig. 3). After that, emissions from small dust grains and PAHs become noticeable around $\lambda = 10\ \mu\text{m}$, since shattering acts as a source of small grains in diffuse regions, and accretion also increases the abundance of small grains (see panels of $t = 0.5\ \text{Gyr}$ in Fig. 4). Finally, the functional shape of the grain size distribution at each region of the ISM converges to the one determined by the balance between shattering and coagulation rate according to the condition of the ISM. Consequently, the emission from large and small grains is relatively prominent in the inner and outer regions of the galaxy, respectively (see panels of $t = 10\ \text{Gyr}$ in Fig. 4).
3. We find that $I_{\nu}(8\ \mu\text{m})/I_{\nu}(24\ \mu\text{m})$ correlates with the PAH mass fraction, but the local radiation field influences it (see Fig. 5). The $8\ \mu\text{m}$ band is almost purely dominated by PAH band emission, while the $24\ \mu\text{m}$ band is contaminated by the emission of large grains, resulting in $I_{\nu}(8\ \mu\text{m})/I_{\nu}(24\ \mu\text{m})$ increasing with the PAH mass fraction. However, stronger radiation fields cause higher dust temperatures, shifting the large

grain emission toward shorter wavelengths and raising the $24\ \mu\text{m}$ emission. consequently, $I_{\nu}(8\ \mu\text{m})/I_{\nu}(24\ \mu\text{m})$ decrease in regions with strong radiation. Hence, $I_{\nu}(8\ \mu\text{m})/I_{\nu}(24\ \mu\text{m})$ can be used as an indicator of the PAH mass fraction with a tendency of underestimating PAH mass fraction in regions with strong radiation.

4. We find that $\nu I_{\nu}(8\ \mu\text{m})/I_{\text{TIR}}$ tightly correlates with the PAH mass fraction and is not affected by the local radiation field (see Fig. 7 and Eq. 9). This is because both total and $8\ \mu\text{m}$ intensities are proportional to the strength of the local radiation field, and hence, the effect of the radiation field is canceled out. Therefore, we suggest that $\nu I_{\nu}(8\ \mu\text{m})/I_{\text{TIR}}$ is a good indicator of the PAH mass fraction in various stages of galaxy evolution.
5. We find that the global PAH mass fraction or $\nu I_{\nu}(8\ \mu\text{m})/I_{\text{TIR}}$ in the entire galaxy evolves with metallicity (see Fig. 8). This is because the interplay between shattering and accretion produces PAHs in the entire galaxy. On the contrary, based on the pixel-based analysis, local $\nu I_{\nu}(8\ \mu\text{m})/I_{\text{TIR}}$ decrease with metallicity in the ISM at higher metallicity ($Z > 0.2\ Z_{\odot}$), while it increases at lower metallicity ($Z \leq 0.2\ Z_{\odot}$). At low metallicity, the metal enrichment causes more efficient shattering, which tends to increase PAHs. At high metallicity, coagulation is rather important in depleting PAHs. We also find that $\nu I_{\nu}(8\ \mu\text{m})/I_{\text{TIR}}$ depends on the gas surface density since the coagulation converts PAHs to large grains in dense ISM. Therefore, the spatially resolved relation of the PAH mass fraction helps us interpret the efficiency of accretion, coagulation, and shattering in various ISM phases.

6. We compare the total SED in the NGC 628-like simulation with the observed one (see Fig. 9). Although dust emission at longer wavelengths of $\lambda \geq 20 \mu\text{m}$ in the simulation is consistent with that in the observations, the PAH emission in the MIR wavelengths in the simulation is lower than that in observations by about 0.5 dex. This result implies that our dust model underestimates PAH masses.
7. We compare the spatially resolved data of $\nu I_{\nu}(8\mu\text{m})/I_{\text{TIR}}$ in the NGC 628-like galaxy simulation and the *Herchel/Spitzer* data (see Fig. 10(a)). We find that the values of $\nu I_{\nu}(8\mu\text{m})/I_{\text{TIR}}$ from the simulation are lower than those from the observations, implying that eight times more PAH mass is required in our simulation.
8. We also compare the spatially resolved data from our simulation to the *JWST* observations with high spatial resolutions (see Fig. 10(b)). We find that R_{PAH} , a PAH indicator composed of *JWST* bands (Eq. 1), decreases with the $21 \mu\text{m}$ intensity in both the simulation and observations. This trend can be explained by the fact that coagulation is more efficient in denser ISM. This comparison also shows that the values of R_{PAH} from the simulation are lower than those from the observation. In our model, coagulation may deplete PAHs too efficiently in dense ISM. Therefore, it may be required to prevent small carbonaceous grains from being lost through coagulation in the ISM.

These results suggest that the spatial comparison between observations and theoretical models using observable signatures of the dust size evolution (e.g., $\nu I_{\nu}(8\mu\text{m})/I_{\text{TIR}}$, $I_{\nu}(8\mu\text{m})/I_{\nu}(24\mu\text{m})$, R_{PAH}) leads us to a quantitative investigation of dust evolution in various ISM while maintaining the original spatial resolution of the observational data. In particular, the comparison with future *JWST* observations for many galaxies with high spatial resolutions will reveal the efficiency of dust processes in the diffuse and dense ISM in various galaxies.

Acknowledgements

KM is a Ph.D. fellow of the Flemish Fund for Scientific Research (FWO-Vlaanderen) and acknowledges the financial support provided through Grant number 1169822N. Numerical computations were carried out on the Cray XC50 at the Center for Computational Astrophysics, National Astronomical Observatory of Japan, and the SQUID at the Cybermedia Center, Osaka University as part of the HPCI system Research Project (hp220044, hp230089). This work is supported in part by the MEXT/JSPS KAKENHI grant numbers 20H00180 and 22K21349 (K.N.), and 21J20930, 22KJ2072 (YO). K.N. acknowledges the support from the Kavli IPMU, World Premier Research Center Initiative (WPI), where a part of this work was conducted. HH thanks the National Science and Technology Council for support through grant 111-2112-M-001-038-MY3 and the Academia Sinica for Investigator Award AS-IA-109-M02. MR acknowledge support from project PID2020-114414GB-100, financed by MCIN/AEI/10.13039/501100011033. SvdG and IDL acknowledge financial support by the European Research Council (ERC) under the European Union's Horizon 2020 research and innovation programme DustOrigin (ERC-2019-StG-851622) and by the Flemish Fund for Scientific Research (FWO-Vlaanderen) through the research project G023821N. We thank Prof. Nakagawa for many fruitful discussions.

References

- Aniano, G., Draine, B. T., Gordon, K. D., & Sandstrom, K. 2011, *PASP*, 123, 1218
- Aniano, G., Draine, B. T., Hunt, L. K., et al. 2020, *ApJ*, 889, 150
- Aniyani, S., Freeman, K. C., Arnaboldi, M., et al. 2018, *MNRAS*, 476, 1909
- Aoyama, S., Hirashita, H., & Nagamine, K. 2020, *MNRAS*, 491, 3844
- Aoyama, S., Hou, K.-C., Shimizu, I., et al. 2017, *MNRAS*, 466, 105
- Asano, R. S., Takeuchi, T. T., Hirashita, H., & Nozawa, T. 2013, *MNRAS*, 432, 637
- Asplund, M., Grevesse, N., Sauval, A. J., & Scott, P. 2009, *ARA&A*, 47, 481
- Baes, M., & Camps, P. 2015, *Astronomy and Computing*, 12, 33
- Baes, M., Gebek, A., Trcka, A., et al. 2024, arXiv e-prints, arXiv:2401.04224
- Baes, M., Verstappen, J., De Looze, I., et al. 2011, *ApJS*, 196, 22
- Berg, D. A., Skillman, E. D., Croxall, K. V., et al. 2015, *ApJ*, 806, 16
- Boquien, M., Calzetti, D., Combes, F., et al. 2011, *AJ*, 142, 111
- Bruzual, G. & Charlot, S. 2003, *MNRAS*, 344, 1000
- Burgarella, D., Nanni, A., Hirashita, H., et al. 2020, *A&A*, 637, A32
- Camps, P. & Baes, M. 2015, *Astronomy and Computing*, 9, 20
- Camps, P. & Baes, M. 2020, *Astronomy and Computing*, 31, 100381
- Camps, P., Baes, M., & Saftly, W. 2013, *A&A*, 560, A35
- Camps, P., Behrens, C., Baes, M., Kapoor, A. U., & Grand, R. 2021, *ApJ*, 916, 39
- Camps, P., Kapoor, A. U., Trcka, A., et al. 2022, *MNRAS*, 512, 2728
- Camps, P., Misselt, K., Bianchi, S., et al. 2015, *A&A*, 580, A87
- Camps, P., Trčka, A., Trayford, J., et al. 2018, *ApJS*, 234, 20
- Cazaux, S. & Tielens, A. G. G. M. 2004, *ApJ*, 604, 222
- Chabrier, G. 2003, *PASP*, 115, 763
- Chang, C.-Y., Huang, Y.-H., Hirashita, H., & Cooper, A. P. 2022, *MNRAS*, 513, 2158
- Chasteney, J., Sandstrom, K., Chiang, I.-D., et al. 2019, *ApJ*, 876, 62
- Chasteney, J., Sutter, J., Sandstrom, K., et al. 2023a, *ApJ*, 944, L11
- Chasteney, J., Sutter, J., Sandstrom, K., et al. 2023b, *ApJ*, 944, L12
- Cherchneff, I., Barker, J. R., & Tielens, A. G. G. M. 1992, *ApJ*, 401, 269
- Chiang, I.-D., Sandstrom, K. M., Chasteney, J., et al. 2018, *ApJ*, 865, 117
- Clark, C. J. R., Verstocken, S., Bianchi, S., et al. 2018, *A&A*, 609, A37
- Conroy, C. 2013, *ARA&A*, 51, 393
- da Cunha, E., Charlot, S., & Elbaz, D. 2008, *MNRAS*, 388, 1595
- Dale, D. A., Cohen, S. A., Johnson, L. C., et al. 2009, *ApJ*, 703, 517
- Davies, J. I., Baes, M., Bianchi, S., et al. 2017, *PASP*, 129, 044102
- Draine, B. T. & Anderson, N. 1985, *ApJ*, 292, 494
- Draine, B. T., Dale, D. A., Bendo, G., et al. 2007, *ApJ*, 663, 866
- Draine, B. T. & Li, A. 2001, *ApJ*, 551, 807
- Draine, B. T. & Li, A. 2007, *ApJ*, 657, 810
- Draine, B. T., Li, A., Hensley, B. S., et al. 2021, *ApJ*, 917, 3
- Dwek, E. 1998, *ApJ*, 501, 643
- Egorov, O. V., Kreckel, K., Sandstrom, K. M., et al. 2023, *ApJ*, 944, L16
- Einasto, J. 1965, *Trudy Astrofizicheskogo Instituta Alma-Ata*, 5, 87
- Galamez, M., Kennicutt, R. C., Calzetti, D., et al. 2013, *MNRAS*, 431, 1956
- Galliano, F., Dwek, E., & Chianial, P. 2008a, *ApJ*, 672, 214
- Galliano, F., Madden, S. C., Tielens, A. G. G. M., Peeters, E., & Jones, A. P. 2008b, *ApJ*, 679, 310
- Galliano, F., Nersesian, A., Bianchi, S., et al. 2021, *A&A*, 649, A18
- Gebek, A., Baes, M., Diemer, B., et al. 2023, *MNRAS*, 521, 5645
- Granato, G. L., Ragone-Figueroa, C., Taverna, A., et al. 2021, *MNRAS*, 503, 511
- Graziani, L., Schneider, R., Ginolfi, M., et al. 2020, *MNRAS*, 494, 1071
- Grieco, F., Orsolini, Y., & Pérot, K. 2023, *Journal of Atmospheric and Solar-Terrestrial Physics*, 252, 106147
- Haardt, F. & Madau, P. 2012, *ApJ*, 746, 125
- Hensley, B. S. & Draine, B. T. 2023, *ApJ*, 948, 55
- Hirashita, H. 1999, *ApJ*, 510, L99
- Hirashita, H. 2012, *MNRAS*, 422, 1263
- Hirashita, H. 2015, *MNRAS*, 447, 2937
- Hirashita, H. 2023, *MNRAS*, 518, 3827
- Hirashita, H. & Aoyama, S. 2019, *MNRAS*, 482, 2555
- Hirashita, H., Deng, W., & Murga, M. S. 2020, *MNRAS*, 499, 3046
- Hirashita, H. & Kuo, T.-M. 2011, *MNRAS*, 416, 1340
- Hirashita, H. & Murga, M. S. 2020, *MNRAS*, 492, 3779
- Hollenbach, D. & McKee, C. F. 1979, *ApJS*, 41, 555
- Hollenbach, D. & Salpeter, E. E. 1971, *ApJ*, 163, 155
- Hou, K.-C., Aoyama, S., Hirashita, H., Nagamine, K., & Shimizu, I. 2019, *MNRAS*, 485, 1727
- Kapoor, A. U., Baes, M., van der Wel, A., et al. 2023, *MNRAS*, 526, 3871
- Kapoor, A. U., Camps, P., Baes, M., et al. 2021, *MNRAS*, 506, 5703
- Kennicutt, Robert C., J. 1998, *ApJ*, 498, 541
- Kennicutt, R. C., Calzetti, D., Aniano, G., et al. 2011, *PASP*, 123, 1347
- Kim, J.-h., Agertz, O., Teyssier, R., et al. 2016, *ApJ*, 833, 202
- Lee, J. C., Sandstrom, K. M., Leroy, A. K., et al. 2023, *ApJ*, 944, L17
- Leja, J., Johnson, B. D., Conroy, C., van Dokkum, P. G., & Byler, N. 2017, *ApJ*, 837, 170

- Leroy, A. K., Schinnerer, E., Hughes, A., et al. 2021, *ApJS*, 257, 43
- Li, A. 2020, *Nature Astronomy*, 4, 339
- Li, A. & Draine, B. T. 2001, *ApJ*, 554, 778
- Lisenfeld, U. & Ferrara, A. 1998, *ApJ*, 496, 145
- Maloney, P. R., Hollenbach, D. J., & Tielens, A. G. G. M. 1996, *ApJ*, 466, 561
- Matsumoto, K., Camps, P., Baes, M., et al. 2023, *A&A*, 678, A175
- Matsuura, M., Bernard-Salas, J., Lloyd Evans, T., et al. 2014, *MNRAS*, 439, 1472
- Matsuura, M., Woods, P. M., & Owen, P. J. 2013, *MNRAS*, 429, 2527
- McKinnon, R., Vogelsberger, M., Torrey, P., Marinacci, F., & Kannan, R. 2018, *MNRAS*, 478, 2851
- Nanni, A., Cristallo, S., Donevski, D., et al. 2023, arXiv e-prints, arXiv:2312.15998
- Narayanan, D., Smith, J. D., Hensley, B., et al. 2023, arXiv e-prints, arXiv:2301.07136
- Navarro, J. F., Frenk, C. S., & White, S. D. M. 1997, *ApJ*, 490, 493
- Nersesian, A., Xilouris, E. M., Bianchi, S., et al. 2019, *A&A*, 624, A80
- Nishida, K. Y., Takeuchi, T. T., Nagata, T., & Asano, R. S. 2022, *MNRAS*, 514, 2098
- O'Donnell, J. E. & Mathis, J. S. 1997, *ApJ*, 479, 806
- Ostriker, J. & Silk, J. 1973, *ApJ*, 184, L113
- Perret, V. 2016, DICE: Disk Initial Conditions Environment, Astrophysics Source Code Library, record ascl:1607.002
- Rau, S.-J., Hirashita, H., & Murga, M. 2019, *MNRAS*, 489, 5218
- Relaño, M., De Looze, L., Saintonge, A., et al. 2022, *MNRAS*, 515, 5306
- Relaño, M., Lisenfeld, U., Hou, K. C., et al. 2020, *A&A*, 636, A18
- Rémy-Ruyer, A., Madden, S. C., Galliano, F., et al. 2015, *A&A*, 582, A121
- Romano, L. E. C., Nagamine, K., & Hirashita, H. 2022a, *MNRAS*, 514, 1441
- Romano, L. E. C., Nagamine, K., & Hirashita, H. 2022b, *MNRAS*, 514, 1461
- Saftly, W., Baes, M., & Camps, P. 2014, *A&A*, 561, A77
- Saftly, W., Camps, P., Baes, M., et al. 2013, *A&A*, 554, A10
- Saitoh, T. R. 2017, *AJ*, 153, 85
- Sandstrom, K. M., Bolatto, A. D., Draine, B. T., Bot, C., & Stanimirović, S. 2010, *ApJ*, 715, 701
- Schreiber, C., Elbaz, D., Pannella, M., et al. 2018, *A&A*, 609, A30
- Seok, J. Y., Hirashita, H., & Asano, R. S. 2014, *MNRAS*, 439, 2186
- Shim, H., Hwang, H. S., Jeong, W.-S., et al. 2023, *AJ*, 165, 31
- Shimizu, I., Todoroki, K., Yajima, H., & Nagamine, K. 2019, *MNRAS*, 484, 2632
- Sloan, G. C., Jura, M., Duley, W. W., et al. 2007, *ApJ*, 664, 1144
- Sloan, G. C., Kraemer, K. E., Wood, P. R., et al. 2008, *ApJ*, 686, 1056
- Sloan, G. C., Lagadec, E., Zijlstra, A. A., et al. 2014, *ApJ*, 791, 28
- Smith, B. D., Bryan, G. L., Glover, S. C. O., et al. 2017, *MNRAS*, 466, 2217
- Springel, V., Pakmor, R., Zier, O., & Reinecke, M. 2021, *MNRAS*, 506, 2871
- Tielens, A. G. G. M. & Hollenbach, D. 1985, *ApJ*, 291, 722
- Trčka, A., Baes, M., Camps, P., et al. 2022, *MNRAS*, 516, 3728
- Vander Meulen, B., Camps, P., Stalevski, M., & Baes, M. 2023, *A&A*, 674, A123
- Vogelsberger, M., McKinnon, R., O'Neil, S., et al. 2019, *MNRAS*, 487, 4870
- Weingartner, J. C. & Draine, B. T. 2001, *ApJ*, 548, 296
- Wolfire, M. G., Vallini, L., & Chevance, M. 2022, *ARA&A*, 60, 247

Table A.1: Morphological parameters of the gas and stellar components in NGC 628-like galaxy simulations

Type	Σ_0 (M_\odot/pc^{-2})	R_e (kpc)	n	b	h_z (kpc)
Star	12	12	1.5	3.9	0.4
Gas	15	6.5	0.5	0.26	0.4

Appendix A: Initial conditions of the NGC 628-like galaxy

We construct the initial condition for the NGC 628-like simulation using the DICE code (Perret 2016), which computes the gravitational potential on a multi-level Cartesian mesh and considers the dynamical equilibrium of multiple material components. We build up the structural properties of the five components: the dark matter halo, stellar disk and bulge, and gaseous disk and halo. First, the total halo is characterized by a virial mass of $1.2 \times 10^{12} M_\odot$, a virial velocity of $v_{200}=150 \text{ km s}^{-1}$, and spin parameter $\lambda = 0.04$. These parameters are determined so that the velocity curve of the simulation is consistent with that of the NGC 628 observations (Aniyan et al. 2018). The dark matter halo with a mass of $1.0 \times 10^{12} M_\odot$ follows the Navarro–Frenk–White (Navarro et al. 1997) profile with the concentration parameter of $c = 25$ and the effective radius of 100 kpc. The gaseous halo follows the same profile but has 1 % of the total mass, $1.2 \times 10^{10} M_\odot$. Second, we obtain the morphological parameters of the gaseous and stellar disk by fitting the observationally estimated radial profiles of the gas and stellar surface density of NGC 628 (S. van der Giessen et al. in prep.) with the Sérsic profile given by,

$$\Sigma(r) = \Sigma_0 \exp\left\{-b_n \left[\left(\frac{r}{R_e}\right)^{1/n} - 1\right]\right\}, \quad (\text{A.1})$$

where r , R_e , Σ_0 , n , and b_n are the radius in the cylindrical coordinate, the half-mass radius, the surface density at the half-light radius, Sérsic index, and a coefficient, respectively. The parameters obtained in the fitting are summarized in Table A.1. Furthermore, we assume the vertical density profile of the galaxy to be the exponential profile defined by

$$\rho(z) \propto \exp(-z/h_z), \quad (\text{A.2})$$

where z and h_z are the height in the cylindrical coordinate and the scale height, respectively. The scale height was obtained from Aniyan et al. (2018). The gaseous and stellar disks have masses of 2.6×10^{10} and $3.5 \times 10^{10} M_\odot$, respectively. Finally, the stellar bulge follows the Einasto profile (Einasto 1965) with a structural parameter of $\alpha = 1.0$ and a mass of $9.26 \times 10^9 M_\odot$.

Appendix B: Various maps of the Milky Way-like galaxy

Figure B.1 shows the maps of the hydrogen surface density, metallicity, local radiation field, and PAH mass fraction, q_{PAH} , (left to right columns) of the Milky Way-like galaxy simulation at $t = 0.5, 1.0, 3.0,$ and 10 Gyr (top to bottom panels). The metallicity and local radiation field are normalized by the Milky Way values. We only show the pixels that satisfy $I_\nu > 0.01 \text{ MJy sr}^{-1}$ at all the *Spitzer* and *Herschel* bands; that is, the pixels used for the analysis (Section 2.2). The maps of the hydrogen surface density show spiral arms and clumps inside the arms, which reflect the resulting complex structures in the ISM containing diffuse and dense regions. In contrast, the metallicity

maps show a smoother axisymmetric gradient in the radial direction. The metallicity reaches the solar one at $t = 10 \text{ Gyr}$ in the entire disk. In the maps of the local radiation field, the star-formation regions associated with stellar clusters along the spiral arms are prominent (redder colors). Given the monotonic decrease in the SFR of the Milky Way-like galaxy, the star-forming regions shrink with time in terms of spatial distributions and sizes. The PAH mass fraction, q_{PAH} , in the entire galaxy increases with time. PAHs are relatively deficient in dense regions, especially in spiral arms and the galaxy center, because of inefficient PAH formation by shattering and efficient PAH depletion by coagulation.

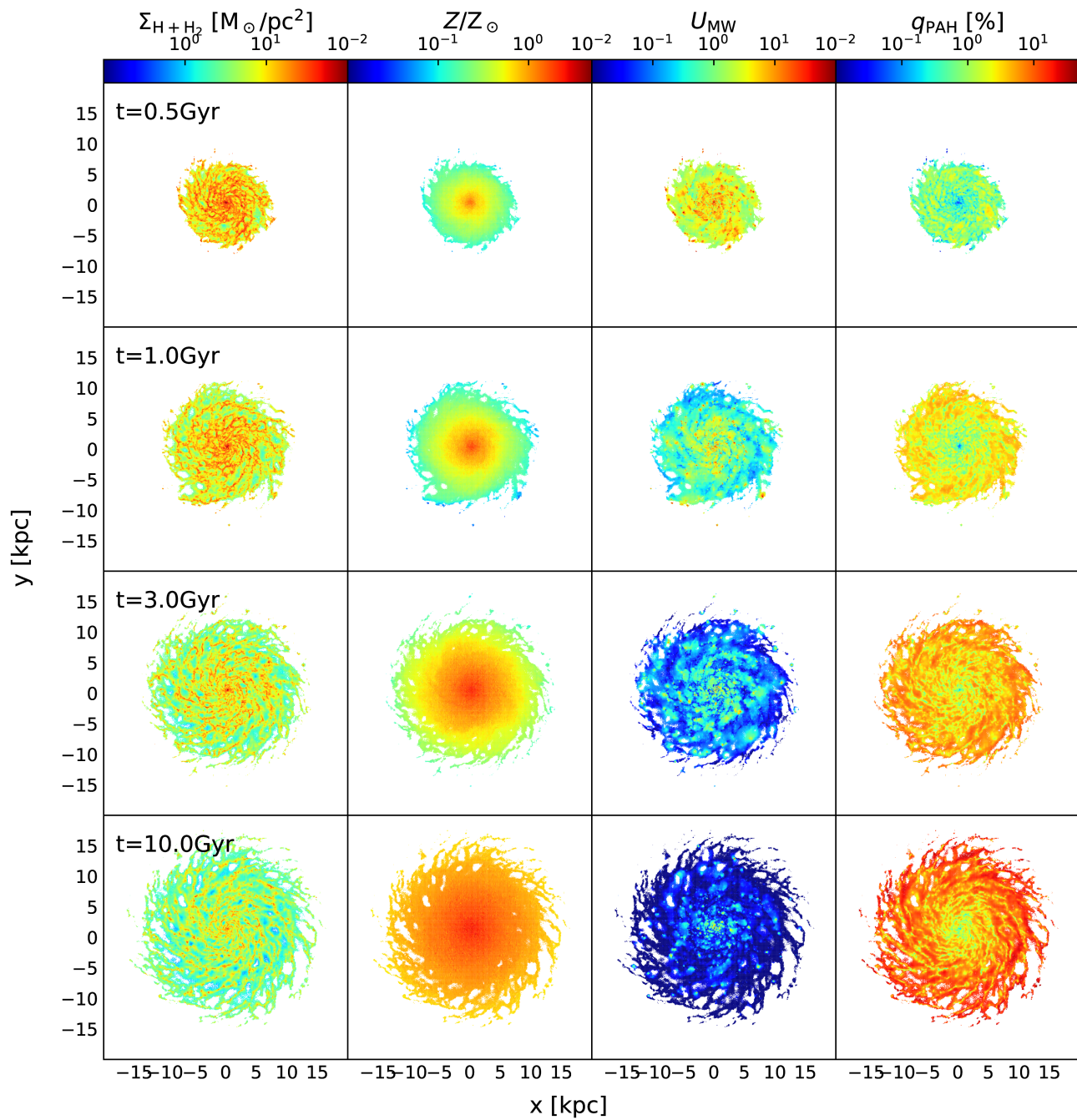


Fig. B.1: Maps of the hydrogen surface density, metallicity, local radiation field, and PAH mass fraction (left to right) of the Milky Way-like galaxy simulation at $t = 0.5$, 1.0, 3.0, and 10 Gyr (top to bottom).